

Physics-based Modeling of Twisted-and-Coiled Actuators Using Cosserat Rod Theory

Jiefeng Sun, *Student Member, IEEE* and Jianguo Zhao, *Member, IEEE*,

Abstract—Twisted and coiled actuators (TCAs) have recently emerged as a promising artificial muscle for various robotic applications because they are strong, low-cost, and customizable. To better facilitate the applications, it is critical to establish general and precise models for different types of TCAs (e.g., self-coiled, free-stroke, conical, etc.). Although several modeling methods have been proposed recently, existing models either fail to capture the nonlinearity during large deformations or cannot model TCAs with non-uniform geometries. In this work, we establish a general framework for modeling TCAs using Cosserat rod theory that can capture the nonlinearity of large deformations and simulate TCAs with non-uniform geometries. Furthermore, we show existing methods are special cases of our general model. Comprehensive statics and dynamics experiments are conducted to verify the proposed model, and the results demonstrate that the model is more accurate than existing ones, especially when a TCA is subject to large deformations. Given the wide applications of TCAs, our general model can help to better design, optimize, and control systems/robots/devices driven by different types of TCAs.

Index Terms—Artificial Muscle, Twisted-and-Coiled Actuators, Statics and Dynamics, Cosserat Rod Theory

I. INTRODUCTION

TWISTED-and-coiled actuators (TCAs) have recently emerged as a promising artificial muscle [1]–[5], exhibiting several unique advantages compared with other types of muscles (e.g., dielectric elastomers, shape memory alloy, liquid crystal elastomer, etc.). They can be conveniently fabricated by continuously twisting polymer fibers into coiled spring-like shapes. They are low cost since the polymer fibers required for fabrication can be commonly used household fibers (e.g., sewing threads or fishing lines). They have a large work density (27.1 kW/kg), capable of lifting more than 1000 times their own weight [1]. They can be directly actuated by electricity with a small voltage (a few volts) [6]. They can also sense their own deformations through the change of electrical properties (e.g., resistance) [7]–[10].

Besides the advantages, TCAs can also be fabricated to have different configurations (Fig. 1) such as self-coiled, free-stroke, conical, etc. Generally, TCAs are fabricated through a two-step process. The first step is the same: twisting a polymer fiber to generate a twisted fiber, whereas the second step differs: using the twisted fiber to generate a coiled shape. Self-coiled TCAs (Fig. 1a) are fabricated by self-coiling in the

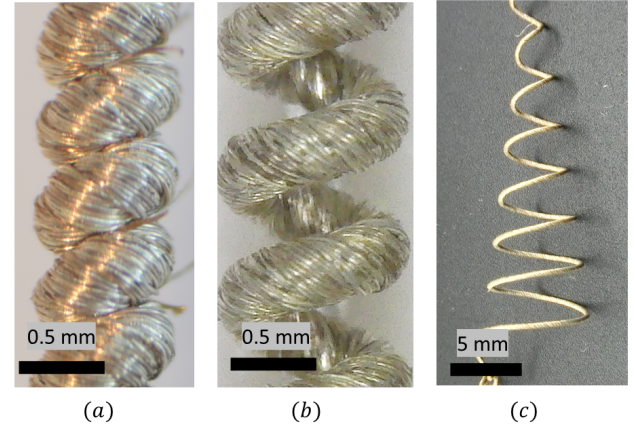


Fig. 1: The photos of three types of TCAs made of conductive sewing threads. (a) Self-coiled TCA. (b) Free-stroke TCA. (c) Conical TCA

second step. Such TCAs can produce large forces but have relatively small strokes (around 10% to 20%) and normally require prestretch before usage [1]. Free-stroke TCAs (Fig. 1b) are fabricated by coiling a twisted fiber along a mandrel with helical grooves in the second step. They can provide moderate actuation forces with relatively large strokes (> 50%) without prestretch [11], [12]. Conical TCAs (Fig. 1c) are fabricated by coiling a twisted fiber along a conical mandrel. They can generate weak forces but with large, even dual-side strokes when the coils pass each other [13].

Due to TCAs' merits and wide customizabilities, they have been recently used in many robotic systems, either rigid or soft/compliant ones. Rigid systems include: an assistive wrist orthosis [14], fingers/hands [15]–[17], a musculoskeletal system [18], a joint mechanism [19], and morphing linkages [20]. Soft/compliant systems include: bending beams [21], soft crawlers [22], [23], soft robotics arms [12], soft skin [24], shape morphing skin [25], and robotic jellyfish [26].

To better design, optimize, and control TCAs for various applications, it is critical to establish precise models for TCAs. A list of existing models are presented in Table I. We are particularly interested in physics-based models based on TCAs' physical parameters as opposed to system identification methods [16], since such physics-based models are expected to be more general. Although some of the existing physics-based models can provide enough accuracy for special types of TCAs (e.g., self-coiled ones), a general model for different types of TCAs (self-coiled, free-stroke, conical) is still missing. In

Manuscript received Feb 22, 2021. Revised June 12, 2021. This work is partially supported by the National Science Foundation under Grant CNS-1755766.

The authors are with the Department of Mechanical Engineering at Colorado State University, Fort Collins, CO, 80523, USA. (Email: j.sun@colostate.edu; jianguo.zhao@colostate.edu)

Reference	TCA type	Twisted Fiber	Thermal Model	Fiber Actuation	Coil Kinematics	Coil Statics	Elastic Moduli
Yang [27]	Self-coiled	Fishing line	None	Concentric helical laminate; CTE d.n. T	CST	CST	Constant
Yip [16], Cho [28], Oiwa [29]	Self-coiled	Sewing thread	Convection	None	Characterized, linear with T	Measured constant	None
Luong [30]	Self-coiled	Sewing thread, Spandex yarn	Convection, damping	None	Characterized linear with T	Measured constant	None
Masuya [31]	Self-coiled	Sewing thread	Convection, radiation, damping	None	Characterized, linear with T	Measured constant	None
Abbas [32]	Self-coiled	Sewing thread	Convection	Single Helix, constant CTE	CST	CST	Calculated, d.n. T
Lamuta [33]	Self-coiled	Carbon Fiber/PDMS	Convection	Fiber radius increase	CST	CST	Calculated constant [34]
Wu [35]	Mandrel-coiled	Sewing thread	None	Convection	Love's Equation	Calculated Constant (Wahl)	Constant
Karami [36]	Self-coiled	Sewing thread	Convection, resistance change	Single Helix, CTE d.n. T	Linear	CST	Calculated d.n. F_e and T
Kotak [37]	Conical	Fishing line	Convection	Single Helix, CTE d.n. T	Linear	Calculated Constant (Wahl)	Constant
Our work	Self-coiled, free-stroke conical	Sewing thread	Convection, monitored power	Single Helix, CTE d.n. T	Cosserat Rod, Love's Equation, CST	Cosserat Rod Love's Equation, CST	Calculated d.n. strain and T

CET: Coefficient of Thermal Expansion; d.n.: depending on; CST: Castigoliano's Second Theorem;

TABLE I: The comparisons between existing models for TCAs

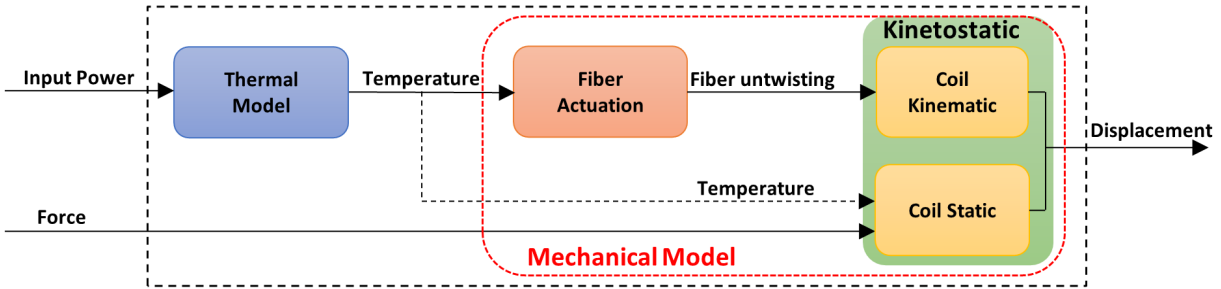


Fig. 2: The schematic for the modeling overview. The input is the input power and the external force, and the output is the TCA's displacement. The whole TCA model is boxed with black dashed lines and the mechanical model is boxed by red dashed lines. The mechanical model can be a TCA statics or TCA dynamics.

the following, we briefly review pioneering works and discuss their limitations.

A. State-of-the-Art for TCA modeling

As shown in Fig. 2, the existing modeling of TCAs can be divided into two sequential models: a thermal model and a mechanical model. The thermal model first solves a TCA's temperature given the input power, and then the mechanical model takes the temperature and external forces to solve the state of the TCA (displacement, velocity, and acceleration, etc.).

For the thermal model, the most common ones treat a TCA as a single body with a uniform temperature, which is the simplest 1D model. This model considers the natural convection in the air as the only energy dissipation, and the heat source is Joule heating from electricity [16], [28]–[30], [32], [33]. In addition to the 1D model, some models consider a more complicated process. Masuya et al. [38] included the radiation and the heat generated from damping to the model.

Karami et al. [36], [39] assumed the resistance of TCAs made of conductive sewing thread linearly changed with respect to temperature.

For the mechanical model, we divide it into three sub-models according to the working principle of TCAs (Fig. 2). As temperature increases, the twisted fiber in a TCA will untwist. A *fiber actuation model* predicts the amount of untwisting with the temperature as an input. With the untwisting, a *coil kinematic model* converts the untwisting to a linear displacement along the TCA. Since TCA has a spring-like helical shape, we need a *coil static model* to predict a TCA's passive deformation under an external load. The coil kinematic and static model, often coupled, together are called a *coil kinetostatic model*.

For the fiber actuation model, there exist extensive works on modeling the untwisting of *monofilament* fibers, such as fishing lines using a single helix model by assuming all the polymer chains in the fiber behave the same like a single helix [40], [41]. However, the actuation of *multifilament* fibers

(sewing threads) is underexplored due to the complicated twisting structure inside them. For instance, a conductive sewing thread (*e.g.*, 235/34 4ply, *Shieldex Trading*) consists of 4 plies of individual yarns twisted together in a ‘z’ twist (right-hand twist), and each yarn is made by twisting *many thin fibers* together in ‘s’ twist (left-hand twist).

For the coil kinematic model, there exist three methods. *The first method is based on system-identification* [16], [28]–[31]. But instead of *measuring* how much a TCA contracts after increasing temperature, the contraction force is *usually* measured. *The other two methods are physics-based*: Castigliano’s Second Theorem (CST) [27], [32] and Love’s equation [6], [13], [35], [42]. CST, based on the infinitesimal strain theory, is usually used to calculate the deformation of a structure under an external load. By considering the untwisting *torque* of a twisted fiber as an external load, CST can relate the untwisting to a TCA’s linear displacement. Love’s equation is a pure kinematic relationship that relates the untwisting of a twisted fiber to a TCA’s pitch angle and thus its displacement. *Note that Knot Theory results in the same kinematic relationship as Love’s equation as discussed by Haines et al. [13]*.

For the coil static model, a TCA’s passive deformation can be determined from its stiffness if we treat the TCA as a mechanical spring. Researchers have used: 1) a constant stiffness obtained from experiments [16], [28]–[30], [43]; 2) a constant stiffness calculated using the classical formula [44] for a helical spring as in [35]; 3) stiffness that varies with deformations [27], [32], [36], [39]. Such nonlinear stiffness has been modeled using CST, but no work *uses* Love’s equation.

Although various models have been proposed recently, they are limited in two aspects. First, they are not general enough for different types of TCAs shown in Fig. 1. In fact, most of the existing models are only *developed for a specific type of TCAs, and there is no existing model that is verified to be able to model different types of TCAs*. Second, existing models are not accurate enough due to modeling simplifications. For example, the CST method is based on the infinitesimal strain (small deformation) theory, and Love’s method ignores the shear and extension strain for the twisted fiber, making them inaccurate when TCAs undergo large deformations.

B. Our Work and Contributions

In this work, we present a general physics-based modeling approach to model a TCA’s statics and dynamics based on the Cosserat rod theory. Cosserat rod theory can accurately model slender rods, including twisted fibers, by considering four strains (torsion, bending, shear, and extension). As a topic in solid mechanics [45], [46], it has been recently adapted to the robotics community to model tendon-driven and fluid-driven compliant/soft robots [47]–[49].

Our proposed model based on Cosserat rod theory is both more accurate and more general compared with existing models. It is more accurate because 1) it is *geometrically exact*: no approximation of small deflection is assumed; 2) it considers all four strains; 3) it can include nonlinearity of material such as temperature and strain dependency. It is also more general because it can model *different types* of TCAs

with different shapes that cannot be modeled using existing models. In fact, we show that existing models using Love’s equation and CST are simplified cases of our model. Because of the *better* generality and accuracy, we expect our model can be widely used for the design and optimization of TCA-actuated devices/systems/robots.

The rest of this paper is organized as follows. In Sec. II, we present the thermal model and the fiber actuation model. In Sec. III, we introduce the Cosserat rod model for coil kinetostatics. In Sec. IV, we show the results using Love’s equation and CST are special cases of our model based on the Cosserat rod theory. In Sec. V, the experimental setup and numerical simulations are introduced. We then compare the simulation and experimental results. In Sec. VI, we briefly discuss the modeling approach. In Sec. VII, we conclude the paper and point out future directions.

II. THERMAL MODEL AND FIBER ACTUATION MODEL

TCAs made of conductive threads are used in this work since they can be directly actuated using electricity and respond much faster than TCAs made of fishing lines wrapped with heating wires. Therefore, our modeling framework starts with a thermal model to obtain a TCA’s temperature given input power, and then a fiber actuation model to predict the amount of fiber untwisting from the temperature increase for the twisted fiber in a TCA.

A. Thermal Model with a Time-varying Input

For TCAs made of conductive threads, their electrical resistance strongly depends on the loading condition and changes over the actuation process ($\sim 20\%$) [9]. Therefore, we cannot assume a constant resistance for modeling. In this case, we directly use the time-varying input power as the real-time input of the thermal model to achieve a better accuracy.

As shown in Fig. 3(a), the 1D thermal diffusion equation is

$$m_t c_p \dot{T} = -hc_s A_0 (T - T_\infty) + P_{in} \quad (1)$$

where T is a TCA’s temperature, the \cdot represents the derivative with respect to time, m_t is the weight of the TCA, c_p is the specific heat, T_∞ is the ambient temperature, h is the natural convection coefficient, and the method to determine h is described in Appendix B-B. $A_0 = 2\pi r_t l_t$ is the surface area of the twisted fiber without considering roughness, with r_t and l_t the diameter and length for the twisted fiber, respectively. $c_s = 2.5$ is used to adjust the surface area due to its roughness (see Fig. 1). In fact, a twisted thread is made of infinite many yarns twisted together, each yarn is made of infinite many thin fibers, and each fiber has a circular cross section. In this case, the outer surface area is scaled up twice, and the scaling factor for each scaling is $\pi/2$, which is the ratio between half perimeter of a circle to its diameter. We calculate h from experimental data using the regression method after c_s is determined. P_{in} is the power input into the TCA that is directly monitored in a control circuit using a sensor (details in Section V-D3). With the initial condition as $T(0) = T_0 = T_\infty$, Eq. (1) can be numerically solved using an ordinary differential equation (ODE) solver in Matlab (e.g., *ode45*).

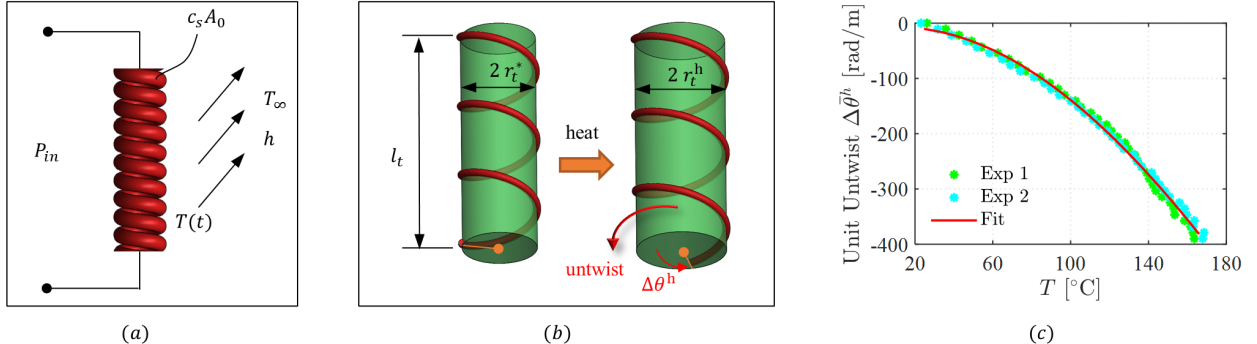


Fig. 3: (a) The schematic for the thermal model. (b) The schematic for the fiber actuation model. The green cylinder represents a twisted fiber. The red helix is a monofiber with a constant length l_f . (c) Experimental and fitted results of the unit untwist of the twisted fiber with respect to temperature.

B. Fiber Actuation Model

After the temperature for a TCA is known, we can solve the amount of untwisting for the twisted fiber in the TCA due to thermal expansion. Such untwisting happens since the twisted fiber expands much more in the radial than the longitudinal direction. Therefore, *given a temperature input*, we first find the radius of the twisted fiber resulted from radial expansion, and then *use the radius to solve the amount of untwisting*.

The twisted fiber's radius r_t^h after heating is an integration of the coefficient of thermal expansion (CTE) in radial direction α_{\perp} :

$$r_t^h = r_t^*(\int_{T_0}^T \alpha_{\perp} dT + 1) \quad (2)$$

where r_t^* and r_t^h are the radius at temperature T_0 and T , respectively. Denote the ratio between r_t^h and r_t^* as $\Gamma(T) = r_t^h/r_t^* = \int_{T_0}^T \alpha_{\perp} dT + 1$. Note that α_{\perp} is not a constant and strongly depends on the temperature [50]. In the rest of this paper, we will use a superscript * to represent the variable in the original reference state (ORS) when no heat and no load is applied, which are fixed parameters that can be measured; we use a superscript h to indicate the variables are corresponding to the heated *reference state (HRS) when the heat is applied but no load is applied*. For example, r_t^* and r_t^h are the twisted fiber's diameter at the *ORS and HRS, respectively*. The variables without the superscript represent a general state when a force is applied *and/or* when the temperature is increased.

To obtain the amount of untwisting from the fiber's radius expansion, we use a single helix model [40], [41]. The model assumes the monofilaments in a twisted fiber form the same helical shape like one single helix wrapped on a cylinder that will expand in the radial direction as shown in Fig. 3(b). The helix satisfies

$$l_f^2 = (r_t^h \theta)^2 + l_t^2 \quad (3)$$

where l_f is the length of the original fiber before twisting, l_t is the length of the helix (the twisted fiber), θ is the total twisting angle: $\theta = 2\pi n_t$ with n_t the number of twists inserted into the twisted fiber.

l_f and l_t can be assumed to be constant since they remain almost the same when the fiber's temperature increases [40].

Therefore, $r_t^h \theta$ will keep constant: $r_t^h \theta = r_t^* \theta^*$. Denote the amount of untwisting due to heat as $\Delta\theta^h$, we can obtain $\Delta\theta^h = \theta^h - \theta^* = \theta^*(r_t^*/r_t^h - 1)$. Further denote the amount of untwisting per unit length as $\Delta\bar{\theta}^h = \Delta\theta^h/l_t$, we have

$$\Delta\bar{\theta}^h = \frac{\theta^*}{l_t} \left(\frac{r_t^*}{r_t^h} - 1 \right) = \frac{\theta^*}{l_t} \left(\frac{1}{\Gamma(T)} - 1 \right) \quad (4)$$

From Eq. (4), we can obtain $\Delta\bar{\theta}^h$ from the radius ratio $\Gamma(T)$, which is challenging to model. Therefore, we use a second-order polynomial $c_2 T^2 + c_1 T + c_0$ to approximate $\Gamma(T)$ and experimentally obtain the coefficients c_i ($i = 0, 1, 2$) by directly monitoring the amount of untwisting for a twisted fiber. Specifically, we first anneal the same twisted fiber for fabricating TCAs shown in Fig. 1 in a straight shape with two ends fixed in an oven (more details in Sec. V-A). The straight twisted fiber is then hanged in an oven, and a 1 g weight is attached at its end to keep the fiber straight. When the oven is gradually heated, a camera is used to capture the fiber's untwisting through the oven's transparent window and a thermal sensor is used to record the temperature. Fig. 3(c) shows the unit untwist with respect to the temperature and the approximation using a second-order polynomial with $c_0 = 3.5 \times 10^{-6}$, $c_1 = -6.7 \times 10^{-5}$, $c_2 = 1$ that provides enough accuracy with an MSRE = 4.1 rad/m, which is 2.3 degrees for a twisted fiber with a length of 1 cm.

With the experimentally obtained $\Gamma(T)$, we can derive the amount of untwisting given a temperature for the twisted fiber using Eq. (4). This amount of untwisting is used as an input for the coil kinetostatic model in the next section.

III. KINETOSTATIC MODEL USING COSSERAT ROD THEORY

The Cosserat rod model can be used to formulate a balance equation between the external wrench (force and moments) and the internal wrench on the twisted fiber in a TCA. In this section, we establish the system of equations of the Cosserat rod model for the kinetostatics of a TCA, derive the moduli of a twisted fiber as a function of temperature and strain, obtain the reference configurations required for numerical

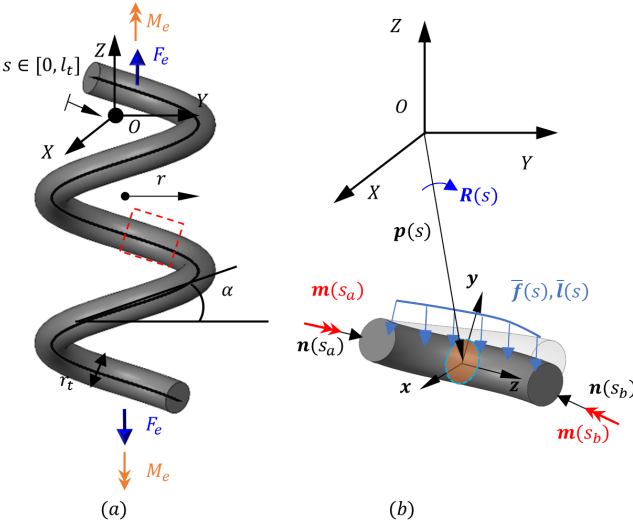


Fig. 4: The schematic for the Cosserat rod model (a) The loading condition of the TCA. The top end is fixed (fixed end), and a force F_e a moment M_e are applied at the bottom end. (b) Arbitrary section of rod (the red box in (a)) from $s = s_a$ to $s = s_b$ subjects to distributed forces \bar{f} and moments \bar{l} . The internal forces n and moments m are also shown.

implementations, and establish a simplified dynamics equation for TCAs.

A. Cosserat Rod Kinetostatic ODEs

The twisted fiber in a TCA can be considered as a slender rod as shown in Fig. 4(a), and the Cosserat rod model [45] assumes the rod is composed of infinitely many rigid cross sections along the rod's centerline defined as the curve passing through the centroids of all the cross sections. We use arc length $s \in [0, l_t]$ to denote the location of a cross section along the centerline.

We establish a global (fixed) frame ($OXYZ$) located at the center of the TCA's fixed end. As shown in Fig. 4(b), we also establish a body frame ($oxyz$) for a rigid cross section at s with o located at the centroid, z direction along the rod's tangent direction, and x, y aligned with the principal axes of the cross section. The orientation of frame $oxyz$ with respect to frame $OXYZ$ can be represented as a rotational matrix $R(s) \in SO(3)$, whereas the position of o in frame $OXYZ$ can be represented as $p(s) \in \mathbb{R}^3$. With $R(s)$ and $p(s)$, we use a homogeneous transformation matrix $g(s) \in SE(3)$

$$g(s) = \begin{bmatrix} R(s) & p(s) \\ \mathbf{0} & 1 \end{bmatrix} \quad (5)$$

to represent the orientation and position of a rigid cross section at s in the global frame.

With the notation in [48], the kinematics of a TCA as a Cosserat rod is $g' = g\hat{\xi}$, where $'$ is the derivative with respect to s , and $\xi = [\mathbf{u}^T, \mathbf{v}^T]^T \in \mathbb{R}^6$ is the spatial twist (strain) representing the relative configuration change between adjacent cross sections along the centerline, with $\mathbf{u} \in \mathbb{R}^3$ and

$\mathbf{v} \in \mathbb{R}^3$ the angular and linear strain component, respectively. The superscript ' T ' denotes the transpose of a matrix. The 'hat' operator $\hat{\cdot}$ is a mapping from \mathbb{R}^3 to $\mathfrak{so}(3)$ or \mathbb{R}^6 to $\mathfrak{se}(3)$, e.g., $\hat{\xi} = \begin{bmatrix} \hat{\mathbf{u}} & \mathbf{v} \\ \mathbf{0} & \mathbf{0} \end{bmatrix}$. We decompose $g' = g\hat{\xi}$ into the angular and linear component to facilitate our numerical simulation using non-unit quaternion (detailed in Section V-B1)

$$\begin{aligned} R' &= R\hat{\mathbf{u}} \\ p' &= R\mathbf{v} \end{aligned} \quad (6)$$

A complete nomenclature is listed in Appendix A.

The statics equation for an arbitrary cross section of the rod as in Fig. 4(b) is

$$\bar{\mathbf{W}}_e - ad_{\xi}^T \mathbf{W} + \mathbf{W}' = 0 \quad (7)$$

where $\bar{\mathbf{W}}_e = [\bar{l}^T, \bar{f}^T]^T$ is the distributed external wrench with $\bar{l}, \bar{f} \in \mathbb{R}^3$ as the moment, force per unit arclength applied to the centerline in the body frame, $ad_{\xi} = \begin{bmatrix} \hat{\mathbf{u}} & \mathbf{0} \\ \hat{\mathbf{v}} & \hat{\mathbf{u}} \end{bmatrix}$ is adjoint representation of the spatial twist ξ . $\mathbf{W} = [\mathbf{m}^T, \mathbf{n}^T]^T$ is the internal wrench in the body frame with $\mathbf{m}, \mathbf{n} \in \mathbb{R}^3$ as the internal moment and force in the body frame.

To relate the kinematic equation (6) and statics equation (7), we can use a constitutive law to relate the internal wrench \mathbf{W} and the change of spatial twist $\Delta\xi = \xi - \xi^*$, where $\xi^* = [\mathbf{u}^{*T}, \mathbf{v}^{*T}]^T$ is the twist in ORS. The change of strains can be caused by the internal forces and moments. For instance, the change of torsional strain $u_z - u_z^*$, where u_z is the third element of \mathbf{u} , can be caused by the moment about the z axis of body frame. More generally, we have the following constitutive law:

$$\mathbf{W} = K\Delta\xi \quad (8)$$

where

$$K = \begin{bmatrix} K_{bt} & 0 \\ 0 & K_{se} \end{bmatrix}$$

$K_{bt} = \text{diag}[EI, EI, GJ]$ is the diagonal stiffness matrix for bending and torsion, and $K_{se} = \text{diag}[GA_t, GA_t, EA_t]$ is the diagonal stiffness matrix for shear and extension. E and G are the longitudinal Young's modulus and shear modulus for the twisted fiber, respectively. A_t is the cross section area of the twisted fiber, $I = I_x = I_y = \pi r_t^4/4$ is the second moment of area, and $J = I_x + I_y$ is the polar moment of inertia of the twisted fiber's cross section about its centroid. A detailed derivation for Eq. (8) using the yarn mechanics is in Appendix B-A

Eqs. (6)-(8) establish the kinetostatics of the TCA together with boundary conditions (the external wrench, e.g., a weight hanging at the TCA's end), creating a boundary value problem (BVP) that can be numerically solved. The actuation of the TCA is realized by replacing \mathbf{u}^* in Eq. (8) with \mathbf{u}^h that can be calculated with the increase of the temperature T (Sec. III-C). Detailed numerical implementations will be presented in Sec. V-B. An animation of TCA simulation can be found in our supporting video. The detailed derivation, source code, and supporting video for this paper are summarized online at <https://jiefengsun.github.io/tca-tro.html>

B. Temperature and Strain Dependent Moduli

The moduli (E and G) of a twisted fiber vary with the temperature and external loads. If such variations are not modeled, we cannot simulate a TCA's response accurately, especially when external loads are large and the temperature is high. To model such variations, we first calculate the moduli at room temperature based on yarn mechanics, and then incorporate the influence of temperature and load.

Moduli of a twisted fiber depend on three parameters of the twisted fiber: the pitch angle α_t , the volume friction V_f , the yarn's (monofilament fiber's) tensile modulus E_f [51]:

$$E = \frac{3V_f E_f}{4} \frac{(1 + \cos^2 \alpha_t)}{1 + \cos \alpha_t + \cos^2 \alpha_t} \quad (9)$$

$$G = E_f V_f / \left(\frac{\pi(1 - \cos \alpha_t) \sin \alpha_t^3}{6(\alpha_t/2 - 1/4 \sin(2\alpha_t))^2} + \frac{8 \sin^3 \alpha_t}{3\pi(1 - \cos \alpha_t)(\cos \alpha_t + 1)^2} + \frac{\pi(4 - 3 \cos \alpha_t - \cos^3 \alpha_t)}{6(\alpha_t/2 - 1/4 \sin(2\alpha_t))(\cos \alpha_t + 1)} \right) \quad (10)$$

Among these three parameters, α_t and V_f can be considered as constants after the annealing process, and they can be experimentally obtained. For α_t , we can directly obtain it from microscopic photos. For V_f , we obtain it indirectly by using Eq. (9) with the values of E and E_f at room temperature. E at room temperature is measured to be 1.2 GPa by stretching an annealed twisted fiber. E_f at room temperature is directly chosen to be $E_f = E_{f0} = 3.9$ GPa, which is the Young's modulus of Nylon 6,6. With E and E_f at room temperature, we solve $V_f = 0.35$ by using Eq. (9).

E_f varies with both external loads and temperature, especially when the load and temperature are large [36], [52]. In our previous work [32], we have considered how E_f will vary with temperature alone: E_f decreases by 0.0011 GPa per Celsius degree. In this work, we also consider the influence of the external load by using a second order polynomial ($\lambda = \mu_2 \tau^2 + \mu_1 \tau + \mu_0$). Therefore, we have

$$E_f = E_{f0} - 0.0011 \Delta T (\mu_2 \tau^2 + \mu_1 \tau + \mu_0) \quad (11)$$

where $\Delta T = T - T_0$ is the change of temperature, $\tau = \frac{F_e r}{G J}$ is the torsional strain induced by an external force F_e along the TCA as shown in Fig. 4(a). Since we don't know the exact G before we calculate τ , we take the value of G at room temperature $G_0 = 0.22$ GPa to calculate τ for a specific load. The coefficients for λ , $\mu_2 = 3.24 \times 10^{-4}$, $\mu_1 = -0.027$, and $\mu_0 = 1$, are fitted using the displacement-force relationship at high temperature and high load condition (see Appendix B-B for more details).

With Eqs. (9)-(11), the moduli (E and G) can be expressed in terms of the temperature and an external force. G is used as an example to illustrate how the modulus will change. We consider the case when we hang a weight at the end of a TCA. We can plot G with respect to temperature and the weight in Fig. 5. The drop of the modulus becomes more than 13% when the temperature and weight both reach a large magnitude. Although we plot G with respect to weights for more intuitive illustrations, it is more general for the moduli to

depend on the torsional strain than the external force produced by hanging weights, since even the same hanging weight at the ends of two TCAs made of the same twisted fiber will cause different torsional strains on the twisted fiber if the two TCAs have different outside diameters.

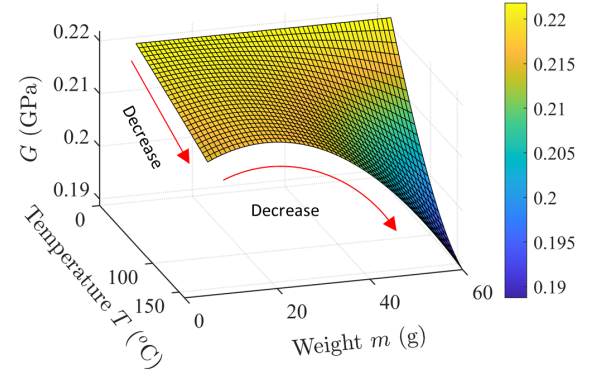


Fig. 5: The change of the shear modulus G with respect to the temperature and hanging weight for a free-stroke TCA fabricated as in Sec. V-A.

C. Reference Strain and Boundary Conditions

To numerically implement the model, we need to obtain the reference strains and the boundary conditions for the two ends. Recall that we define two types of reference states: 1) a TCA's original reference state (ORS) when no load and no heat is applied; 2) a heated reference state (HRS) when the heat is applied but no load is applied. We use a superscript * and h to represent ORS and HRS, respectively. For instance, a TCA may initially have an ORS strain ξ^* when no load and heat is applied, but when the heat is applied, ξ^* will be shifted to an HRS strain ξ^h .

Here we use a right-handed TCA as an example to obtain the references, and the derivation for a conical TCA is discussed in Appendix B-C. The derivations are also implemented using Matlab Symbolic Toolbox, and the source code can be found at <https://github.com/jiefengsun/TCA-TRO>. The TCA is hanged by fixing its top, and the global frame's origin O is established at the top of the TCA as shown in Fig. 4(a). Z direction is along the axis of the TCA. In the following, we will obtain the relative position and orientation for a cross section in the twisted-fiber with respect to the global frame (i.e., frame $oxyz$ with respect to frame $OXYZ$ in Fig. 4(b)).

The position vector $\mathbf{p}^*(s)$ in ORS can be parameterized using arc-length as

$$\mathbf{p}^*(s) = [r^* \cos(\phi), r^* \sin(\phi), s \sin(\alpha^*)]^T \quad (12)$$

where $\phi = 2\pi n = s \cos \alpha^*/r^*$ is the coiling angle, n the number of coils, r^* the radius of the coil, and α^* the pitch angle in ORS.

The rotation matrix $R^*(s)$ in ORS can be also parameterized using s through consecutive frame transformations as shown in Fig. 6.

$$R^*(s) = \textcolor{orange}{R}_z(\pi - \phi) \textcolor{green}{R}_x(-\frac{\pi}{2} - \alpha^*) \quad (13)$$

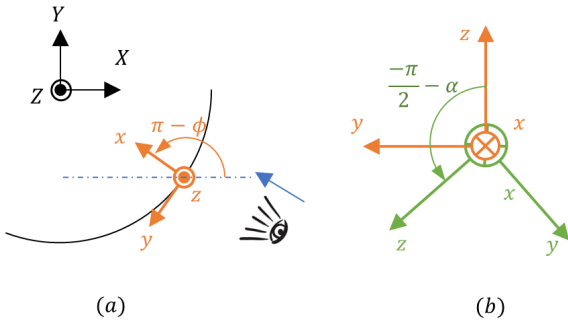


Fig. 6: The steps to obtain the rotational matrix $R^*(s)$. (a) The top view for the first step rotating around z for $\pi - \phi$. (b) The view for the second step looked from the arrow direction in (a). Rotate around x for $-\frac{\pi}{2} - \alpha^*$ with respect to the body frame. Signs of the rotation angles are determined using the right hand rule.

where R_x, R_z are respectively basic rotation matrices that rotate frames about the x -, or z -axis by an angle using the right-hand rule. The colored item in Eq. (13) is corresponding to the body frame in the same color after rotation in Fig. 6. Note that post multiplication is used (rotation with respect to the current body frame) and the final z orientation of the body frame is always along the tangent direction of the twisted fiber. A 3D animation of the body frame moving along a helix is shown in the supporting video.

With $p^*(s)$ and $R^*(s)$, we can then obtain the ORS strain u^* and v^* from Eq. (6)

$$\begin{aligned} u^*(s) &= (R^{*T} R'^*)^\vee = [0, \kappa^*, \tau^*]^T \\ v^* &= R^{*T} p'^* = [0, 0, 1]^T \end{aligned} \quad (14)$$

where $\kappa^* = \cos^2 \alpha^*/r^*$, $\tau^* = \sin \alpha^* \cos \alpha^*/r^*$ are the geometric curvature and torsion of the helix. Note that v^* does not vary with geometry parameters.

When heated, the twisted fiber untwists, the ORS strain is shifted to the HRS strain by adding the influence of untwisting to the geometric torsion

$$u^h(s) = [0, \kappa^*, \tau^* + \Delta\bar{\theta}^h]^T, \quad v^h = v^* \quad (15)$$

Note that $\Delta\bar{\theta}^h$ changes with respect to temperature T ; therefore, u^h is a function of T . In the simulation, u^h is iteratively updated based on the temperature to incorporate the thermal actuation.

After solving the reference strains, we can solve the boundary conditions. We first derive the boundary condition for the fixed end of a TCA's whose centerline is along the global Z axis. We will then discuss the boundary conditions for the free end with a external load applied on it.

The boundary condition for the fixed end ($s = 0$) can be solved from Eqs. (12) and (13)

$$\begin{aligned} p_0 &= p^*(0) = [r^*, 0, 0]^T \\ R_0 = R^*(0) &= \begin{bmatrix} -1 & 0 & 0 \\ 0 & \sin(\alpha^*) & -\cos(\alpha^*) \\ 0 & -\cos(\alpha^*) & -\sin(\alpha^*) \end{bmatrix} \end{aligned} \quad (16)$$

The boundary condition for the free end with an external wrench W_e^g (superscript ' g ' means it is in the global frame) at $s = l_t$ is

$$W(l_t) = Ad_{g(l_t)}^T W_e^g \quad (17)$$

where

$$Ad_g = \begin{bmatrix} R & 0 \\ \hat{p}R & R \end{bmatrix}$$

is the adjoint representation for the Lie group element g , Ad_g^T will transform W_e^g to the body frame. When a weight m is hanged at the TCA's end, $W_e^g = [0, 0, 0, 0, 0, -mg_r]^T$ with $g_r = 9.81 \text{ m/s}^2$ the gravitational constant.

D. Modeling TCA Dynamics using Cosserat Rod Kinetostatic Model

TCAs are generally used for actuation (e.g., lifting weights). In this case, we can simplify its dynamics model by ignoring the inertial force of a TCA since the hanging weight is usually over 1000 times heavier than a TCA's weight. In other words, we can establish a simplified dynamics model based on the Cosserat rod kinetostatics. Such a simplification can reduce the Cosserat rod dynamics, which is a system of partial differential equations (PDEs) with respect to time and space, to an ODE with respect only to time:

$$m\ddot{x} + b_t\dot{x} + f_{rod}(x, T(t)) = 0 \quad (18)$$

where x is the displacement of the weight m from the loaded equilibrium, the \cdot is the derivative with respect to time, b_t is the damping coefficient of the TCA, $f_{rod}(x, T(t))$ is the TCA's internal force calculated from the Cosserat rod model for a displacement x and temperature $T(t)$.

IV. SIMPLIFICATION AND SPECIAL CASES

In this section, we show that existing models (e.g., Love's equation and CST) for the kinetostatics of TCAs can be considered as special cases of the more general Cosserat rod model aforementioned.

A. TCA Kinetostatic Modeling with Love's Equation

Love's equation [42] establishes the kinematic relationship between a helix's pitch angle and its precursor fiber's torsion change, which has been proposed for modeling TCAs [13], [35]. But the equation is a special case of Cosserat rod model in terms of a helix. In fact, a Cosserat rod model can be reduced to a Kirchhoff rod model by ignoring the shear and extension strains, and then the Kirchhoff rod model can be further reduced to Love's equation. Without shear and extension, a helical TCA will have constant geometric curvature and torsion anywhere along the centerline (i.e., u does not depend on s) if the external force is along the centerline. Therefore, if we denote the third element of $u^h(s)$ in Eq. (15) as τ^h , then we have $\tau^h = \tau^* + \Delta\bar{\theta}^h$ for any point of the helix. This can be rearranged to

$$\Delta\bar{\theta}^h = \frac{\sin \alpha^h \cos \alpha^h}{r^h} - \frac{\sin \alpha^* \cos \alpha^*}{r^*} \quad (19)$$

which is the same form of Love's equation as in Ref. [1], [13], [35].

Previous works only use Love's equation for the coil kinematic model and need to rely on other coil static models (e.g., CST or a constant stiffness coefficient) [13], [35] to complete a TCA model (*Table I*). Here, we will directly use Love's equation to establish the statics model for TCAs.

When an external wrench \mathbf{W}_e^g in the global frame is applied to a TCA and the wrench's axis coincides with the TCA's axis as shown in Fig. 4(a), the corresponding internal wrench \mathbf{W} in the body frame will not vary with respect to s due to the symmetry of the geometry around the axis of \mathbf{W}_e^g . Therefore, \mathbf{W} at any s is equal to the value at boundary, which can be calculated using the boundary condition Eq. (17)

$$\mathbf{W} = \mathbf{W}(0) = Ad_{g0}^T \mathbf{W}_e^g \quad (20)$$

where

$$Ad_{g0} = \begin{bmatrix} R_0 & 0 \\ \hat{\mathbf{p}}_0 R_0 & R_0 \end{bmatrix} \quad (21)$$

R_0 and \mathbf{p}_0 are from Eq. (16), $\mathbf{W}_e^g = [\mathbf{M}_e^T, \mathbf{F}_e^T]^T$, \mathbf{F}_e and \mathbf{M}_e are respectively the external force and moment vectors, $\mathbf{F}_e = [0, 0, F_e]^T$, $\mathbf{M}_e = [0, 0, M_e]^T$ with F_e and M_e that are respectively the force and moment applied at the free end. For a hanging weight, $F_e = -mg_r$ and $M_e = 0$. Note that there is no need to distinguish the boundaries at the two ends, i.e., $Ad_{g0} = Ad_{g(l_t)}$.

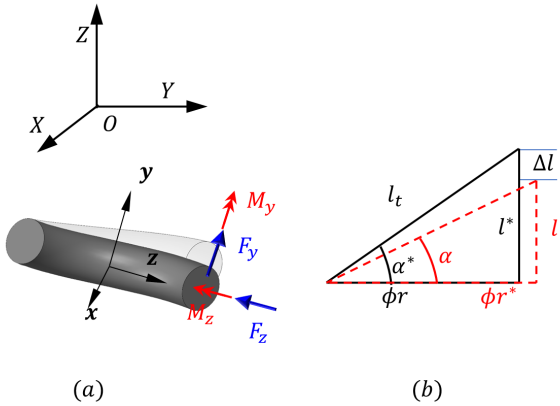


Fig. 7: (a) The wrench in the body frame (F_x and M_x are not shown since they are zero). (b) The geometric relation of a helical TCA before and after deformation

Therefore, $\mathbf{W} = [\mathbf{m}^T, \mathbf{n}^T]^T$ with $\mathbf{m} = [M_x, M_y, M_z]^T$ and $\mathbf{n} = [F_x, F_y, F_z]^T$ as shown in Fig. 7(a) can be expressed as:

$$\begin{aligned} M_x &= 0 \\ M_y &= F_e r \sin \alpha - M_e \cos \alpha \\ M_z &= -F_e r \cos \alpha - M_e \sin \alpha \\ F_x &= 0, F_y = -F_e \cos \alpha, F_z = -F_e \sin \alpha \end{aligned} \quad (22)$$

After ignoring shear and extension, the constitutive law of the Cosserat rod Eq. (8) can be reduced as $\mathbf{m} = K_{bt}(\mathbf{u} - \mathbf{u}^h)$, which can be decomposed to

$$\Delta\kappa = \frac{M_y}{EI}, \quad \Delta\tau = \frac{M_z}{GJ} \quad (23)$$

where $\Delta\kappa = \kappa - \kappa^h = \cos^2 \alpha / r - \cos^2 \alpha^h / r^h$, and $\Delta\tau = \tau - \tau^h = \sin \alpha \cos \alpha / r - \sin \alpha^h \cos \alpha^h / r^h$

Since the TCA's unwinding at the end is negligible, the total coiling angle is a constant (ϕ does not change as in Fig. 7(b)):

$$\frac{\phi}{l_t} = \frac{\cos \alpha}{r} = \frac{\cos \alpha^h}{r^h} = \frac{\cos \alpha^*}{r^*} \quad (24)$$

Substituting M_z and M_y from Eq. (22) into Eq. (23) and using Eq. (24), we have

$$\begin{aligned} F_e + \frac{GJ \cos^2 \alpha^*}{r^{*2}} (\sin \alpha - \sin \alpha^h) \\ - \frac{EI \tan \alpha \cos^2 \alpha^*}{r^{*2}} (\cos \alpha - \cos \alpha^h) = 0 \end{aligned} \quad (25)$$

We also have the following relationship for a TCA's length as shown in Fig. 7(b)

$$l = l_t \sin \alpha \quad (26)$$

Using Eqs. (19), (25), (26) and simplifying, we can get the displacement $\Delta l = l^* - l$ shown in Fig. 7(b) as a function of external force F_e and the unit untwist $\Delta\bar{\theta}^h$ due to heat

$$\Delta l = \frac{1}{K_{lv}} F_e - A_{lv} \Delta\bar{\theta}^h \quad (27)$$

where

$$\begin{aligned} \frac{1}{K_{lv}} &= \frac{l_t(r^h)^2}{GJ \cos^2 \alpha^h + EI \tan \alpha \frac{\cos \alpha^h - \cos \alpha}{\sin \alpha - \sin \alpha^h}} \\ A_{lv} &= \frac{l_t r^*}{\cos \alpha^*} \end{aligned}$$

B. TCA Kinetostatic Modeling with Infinitesimal Strain Theory

CST has been widely used to model a TCA's kinetostatics [27], [32], [33], [36], but the results from CST can be considered as a linearized case of the Cosserat rod model by loosening the geometry exactness using 'small deformation' approximation (Infinitesimal strain theory) – assuming the deformed shape is close to the initial shape.

The actuation is considered as an external force, $M_a = \Delta\bar{\theta}^h GJ$ applied along z axis; therefore, $M_z = -F_e r \cos \alpha - M_e \sin \alpha + M_a$ in \mathbf{W} (Eq. (22)). Inverse the constitutive law Eq. (8) to get $\Delta\xi = K^{-1}\mathbf{W}$, which is the strain in the body frame, and it can be transformed to the global frame due to the small deformation assumption.

$$\Delta\xi^g = Ad_{g0} \Delta\xi \quad (28)$$

The sixth element of $\Delta\xi^g$ is $\Delta\xi_6^g$, which represents the TCA's linear strain along the global Z axis. Integrating the strain over the arc-length results in the TCA's linear displacement. Since $\Delta\xi_6^g$ is independent of the arc-length s , we have a form similar to Eq. (27) but with different coefficients

$$\Delta l = l_t \Delta\xi_6^g = \frac{1}{K_{cst}} F_e - A_{cst} \Delta\bar{\theta}^h \quad (29)$$

where

$$\begin{aligned} \frac{1}{K_{cst}} &= l_t \left(\frac{r^2 \cos^2 \alpha}{GJ} + \frac{r^2 \sin^2 \alpha}{EI} + \frac{\cos^2 \alpha}{GA_t} + \frac{\sin^2 \alpha}{EA_t} \right) \\ A_{cst} &= l_t r \cos \alpha \end{aligned}$$

Note that based on the small deformation assumption, all the variables are close to their values of the reference states, for example, $\alpha \approx \alpha^* \approx \alpha^h$. Although we don't distinguish them in Eq. (29), the results' accuracy could be improved by iteratively updating the variables based on the previous step or using an implicit solver, which can be observed in our supporting code.

Eq. (29) is the same as the results from CST, which is discussed in Appendix B-C, and it can be used to calculate a TCA's deformation when F_e and $\Delta\bar{\theta}^h$ are known. From Eqs. (27) and (29), it is clear that a TCA's deformation comes from two sources: the external load F_e and unit untwist $\Delta\bar{\theta}^h$ resulted from thermal expansion.

C. Dynamics for Love's and CST Methods

Although Eqs. (27) and (29) are convenient for calculating the static deformation, we rearrange them to an equilibrium of forces to facilitate the extension to dynamics

$$F_e + K_c(\Delta l - A\Delta\bar{\theta}^h) = 0 \quad (30)$$

where K_c can be K_{lv} or K_{cst} , and A can be A_{lv} or A_{cst} . We call A the coil kinematic coefficient and K_c the coil stiffness coefficient.

For the most common scenario when a weight is hanged at the end of a TCA, the dynamics model can be easily extended from a statics model by including damping force and inertial force ($F_e = m\ddot{x} + b_t\dot{x} + mg_r$)

$$m\ddot{x} + b_t\dot{x} - K_c A \Delta\bar{\theta}^h = 0 \quad (31)$$

Note that x is the displacement of the weight from the loaded equilibrium, and we use $\Delta l K_c = -mg_r$, when Δl is the displacement from the natural equilibrium (no load) to the loaded equilibrium.

V. SIMULATION AND EXPERIMENTAL RESULTS

In this section, we experimentally validate our model and compare its accuracy with existing models under different loading scenarios for the self-coiled and free-stroke TCAs. We also demonstrate our model can model conical TCAs.

A. Fabrication of TCAs

We fabricate three types of TCAs: a self-coiled TCA, a free-stroke TCA, and a conical TCA. In the following, we briefly describe the fabrication process.

The three types of TCAs have the same twisted fibers. Since it is made from threads, we will use twisted threads in the rest of this section. To fabricate the twisted thread, we hang a weight of 240 g at the end of a sewing thread (Shieldex Trading, 235/36 dtex 4 ply HC+B) and twist it until reaching the verge of self-coiling by inserting unit twist 4.71 rad/mm. A weight heavier than 240 g may easily break the threads, and a lighter weight will not allow for enough twisting of the threads. The unit twist in the twisted threads for the three TCAs are the same, and the parameters of the twisted threads are listed in Table II.

The self-coiled TCA is fabricated by continuously inserting twisting to the twisted thread. To make sure the prescribed

Item	Unit	Value
Inserted torsion for annealing θ^*	rad/mm	4.71
Twisted fiber radius r_t^*	mm	0.21
Twisted fiber pitch angle α_t	°	40
Volume Friction		0.35
Specific heat c_p	J/(Kg K)	1267
Density ρ	kg/m ³	1300
Convection Coefficient h	W/(m ² K)	30
Ambient Temperature $T_\infty = T_0$	° C	25
Longitudinal Young's modulus E	GPa	Eq. (9)
longitudinal shear modulus G	GPa	Eq. (10)
Thermal actuation	rad/mm	Eq. (4)

TABLE II: The parameters of the twister fiber for all the TCAs.

Item	Unit	Self-coiled	Free-stroke	Conical
Precursor fiber length	mm	218	218	181
Twisted fiber length l_t	mm	175	175	145
TCA made length	mm	56	66.75	57
TCA natural length l^*	mm	56	45	55
Number of coils n		120	63	5.3
Coil radius r^*	mm	0.227	0.408	nc*
Pitch angle α^*	°	18.66	22.42	nc*

* Nonconstant

TABLE III: The parameters of the self-coiled TCA, free-stroke TCA, and the conical TCA

amount of twist is inserted in the twisted thread, we manually trigger the self-coiling process by reducing the hanging weight from 240 g to 210 g and manually disturbing the thread. After the first coil is triggered, we continuously insert twisting to the thread to finish the coiling process.

The free-stroke TCA is fabricated by coiling the twisted thread in the groove of a helical mandrel. The helical mandrel is fabricated by wrapping a thin copper wire on a mandrel core (thick copper wire) in a helical shape with a pitch angle of 22.42 ° as shown in Fig. 8(a). A customized machine is used, and the detailed fabrication process of free-stroke TCAs can be found in [12].

The conical TCA is fabricated by coiling the twisted thread

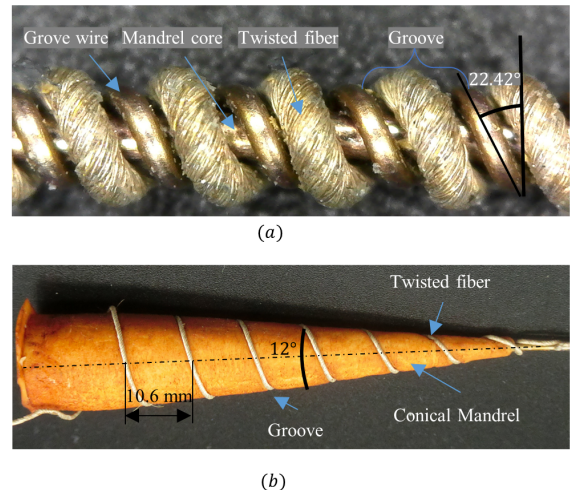


Fig. 8: (a) The helical mandrel with the coiled free-stroke TCA. (b) The conical mandrel with the conical TCA.

on a conical spiral mandrel (Fig. 8(b)) made of *heat-resistant* material (EpoxAcast 670 HT, Smooth-On, Inc.). The conical mandrel is a copy of our 3D printed conical mandrel (Objet30, Stratasys Ltd.), because the 3D printed part is not heat resistant. The copying procedure is 1) fabricating a mold using the 3D printed part and silicone rubber (Mold Max 29NV, Smooth-On, Inc.); 2) casting the EpoxAcast 670 HT to the mold; 3) demolding the mandrel and doing a heat treatment before use. The conical spiral groove in the conical mandrel has a constant pitch $p_c = 10.6$ mm and a cone angle 12° that results in $a = 2\pi/p_c$ and $b = \tan(12\pi/360)$ for the conical spiral's curve equation Eq. (36) in the Appendix.

The three types of TCAs' ends are constrained and annealed in an oven (10GCE, Quincy Lab, accuracy 0.5°C) for 2.5 hours at a temperature of 185°C , which will stabilize the shapes. Finally, the free-stroke TCA and conical TCA are removed from the mandrels. The parameters of the three TCAs are listed in Table III.

B. Numerical Implementations for the Cosserat Rod Model

1) *Quaternions as Rotation:* Spatial derivative of rotations (R') is integrated using non-unit quaternions to avoid truncation error and ensure $R \in \text{SO}(3)$ [53]. This method allows any high-order integration scheme or general purpose ODE solver to efficiently integrate rotations over long spatial range while eliminating singularities and maintaining the structure of $\text{SO}(3)$. The basic idea is to represent R using a quaternion \mathbf{h} , and represent R' using \mathbf{h}' and \mathbf{u} , then the integration of R' can be performed by integrating \mathbf{h}' .

A quaternion $\mathbf{h} = h_0 + h_1i + h_2j + h_3k$, where i, j , and k are called quaternionic units. \mathbf{h} can be written in a vector form in \mathbb{R}^4 : $\mathbf{h} = [h_0, h_1, h_2, h_3]^T$. Then we can have the derivative of \mathbf{h} with respect to s as [53]

$$\mathbf{h}' = \frac{1}{2} \begin{bmatrix} 0 & -u_x & -u_y & -u_z \\ u_x & 0 & u_z & -u_y \\ u_y & -u_z & 0 & u_z \\ u_z & u_y & -u_x & 0 \end{bmatrix} \begin{bmatrix} h_0 \\ h_1 \\ h_2 \\ h_3 \end{bmatrix} \quad (32)$$

where u_x, u_y and u_z are 3 elements of \mathbf{u} . We can calculate rotational matrix R using \mathbf{h} , and use R in kinematic calculation

$$R(\mathbf{h}) = I + \frac{2}{h^T \mathbf{h}} \begin{bmatrix} -h_2^2 - h_3^2 & h_1h_2 - h_3h_0 & h_1h_3 + h_2h_0 \\ h_1h_2 + h_3h_0 & -h_1^2 - h_3^2 & h_2h_3 - h_1h_0 \\ h_1h_3 - h_2h_0 & h_2h_3 + h_1h_0 & -h_1^2 - h_2^2 \end{bmatrix} \quad (33)$$

It is also useful to calculate \mathbf{h} from a rotational matrix R to obtain the initial condition. A robust numerical scheme [54] is implemented in Matlab as *quat2rotm* function, and we use it in our numerical simulation to find $\mathbf{h}_0 = \text{quat2rotm}(R_0)$.

2) *Finite Difference Solver:* Eqs. (6)-(8) together with boundary conditions Eqs. (16) and (17) represent a boundary value problem (BVP) that can be solved by two typical methods: shooting methods or finite difference methods. A shooting method iteratively guesses the unknown boundary values for the fixed end (initial boundary) and evaluates the boundary values at the other end after numerical integration,

which is fast for certain problems [49]. However, we found that the shooting method *couldn't* provide *good* initial guesses for a complicated shape such as TCAs with many coils. Therefore, we use a finite difference solver in Matlab *bvp5c* for the BVP [55].

3) *Simulation Process of TCA Statics:* For a simple case where a weight is hanged at the end of a TCA and then lifted up, the simulation process is shown in Algorithm 1.

Algorithm 1: TCA statics with a hanging weight.

```

Input: Weight  $m$  and maximum temperature  $T_{max}$ 
Initialize geometric parameters and loading;
Setup boundary conditions  $R_0, p_0, \mathbf{W}(l_t)$ ;
Solve rod ODEs for loaded equilibrium before heating;
for  $T = T_0 \rightarrow T_{max}$  do
    Obtain unit untwists  $\Delta\bar{\theta}^h$  (Eq. (4));
    Update the HRS strain  $\xi^h$  (Eq. (15));
    Update moduli  $E$  and  $G$  (Eq. (9)-(11));
    Solve rod BVP for the actuation;
    Extract the displacement  $x$ ;
    Visualization;
end

```

The program has two inputs: the maximum temperature and the weight. It begins with declarations of the various physical parameters. Then, it solves the static equilibrium of the TCA with weight at the end before increasing temperature. In the main loop, each step, it updates the corresponding unit untwist $\Delta\bar{\theta}$ (Eq. (4)), the HRS strain (Eq. (15)), and material modulus (Eqs. (9) - (11)) according to the temperature increase. After that, it solves the BVP (Eqs. (6) - (8), (16) and (17)) with visualization of results.

4) *Simulation Process of TCA Dynamics:* We solve Eq. (18) using the finite difference method combined with the shooting method. The shooting method first guesses and then solves the internal force of the rod $f_{rod,i}$ for time step i , that minimize the residual $res_i = |f_{rod,i} - m\ddot{x}_i - b\dot{x}_i|$, using central difference schemes [56]

$$\ddot{x}_i = \frac{x_{i+1} - 2x_i + x_{i-1}}{\Delta t^2}, \dot{x}_i = \frac{x_{i+1} - x_{i-1}}{2\Delta t}$$

where Δt is the time step size, $i \in \{1, \dots, N_s\}$ is index of the time step, and N_s is the total number of time steps. The displacement x_i is solved as an intermediate variable. Detailed explanation and the source code are available online at <https://github.com/jiefengsun/TCA-TRO>

C. Numerical Schemes for Love's and CST Methods

The numerical scheme for the two methods is the same. A general statics simulation scheme is boxed in the green area in Fig. 9. First, a temperature T is input into the fiber actuation model to obtain the unit untwisting $\Delta\bar{\theta}^h$ of the twisted fiber, and then $\Delta\bar{\theta}^h$ is input into the coil kinematic model to obtain the displacement and pitch angle due to actuation. Given an external force F_e , the final displacement Δl can be calculated from the coil static model by solving

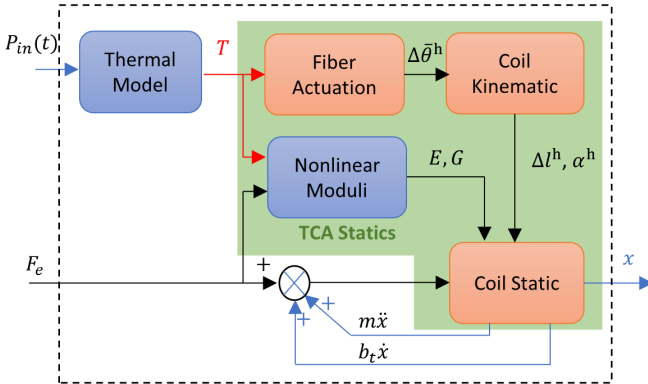


Fig. 9: The schematic of the TCA's dynamics model. The green shaded area is a schematic of the static model with T and F_e as the input, and Δl as output.

the equilibrium equation with the nonlinear moduli (E and G) influenced by the temperature.

A general dynamics simulation scheme is shown in Fig. 9 as boxed by black dashed lines. The model takes time-varying electric power $P_{in}(t)$ as the input to solve the temperature T using the thermal model. Then T is input into the static model. In addition to a static external force F_e , time-varying load such as inertial force ($m\ddot{x}$) and damping force ($b_t\dot{x}$) are implicitly calculated using the same method as the rod dynamics.

D. Kinetostatics and Dynamics of Self-coiled and Free-stroke TCAs

To compare the accuracy of various methods, three cases of simulations and experiments are conducted for the self-coiled TCA and the free-stroke TCA.

1) Considerations on the Experiments and Simulation: Due to the viscoelastic effect of the nylon 6,6 material, a TCA will gradually elongate to another length corresponding to the load applied to it after a certain time or through a few heating cycles known as creep [57], [58]. ‘Lonely stroke’ is used to describe the phenomenon that a TCA’s displacement will be influenced by its time history of loading [59].

While the equilibrium length at a certain time cannot be predicted without considering viscoelasticity, most applications of TCAs only consider the actuation displacement of the TCAs starting from an equilibrium length, which can be easily measured in applications, especially when closed-loop control is required. In this work, we conduct experiments starting at such an equilibrium state as if the TCA has already crept to the length corresponding to the weight. We also use the reference state corresponding to the length as the reference for simulation.

A helical TCA will stop contraction when neighboring coils contact each other. Therefore, its stroke is mainly limited by coil contact, especially when the load is small. For some applications, prediction of contact is preferred. As a general modeling framework, we consider the coil contact by using a Sigmoid (Logistic) function to reduce $\Delta\bar{\theta}^h$, once $\alpha < \alpha_{min}$,

let $\Delta\bar{\theta}^h = \Delta\bar{\theta}^h + 20e^{50(\alpha_{min}-\alpha)}$, where α_{min} is calculated by measuring the minimum length of a TCA.

We study three most common application scenarios for helical TCAs: 1) *kinetostatics* with a hanging-weight, 2) explicit known varying load, and 3) dynamics of with a hanging-weight. Each type of experiment is repeated three times and the mean value and standard deviation are respectively plotted as a solid line and the corresponding shaded area.

2) *Case 1: Kinetostatics with a Hanging Weight*: We first evaluate the kinetostatics when we hang a weight at the end of a TCA by gradually increasing the TCA's temperature. Such an experiment is a common case for TCAs. In fact, most of references in Table I use this case to verify their models. Our experimental setup is shown in Fig. 10(a). The TCA's top is fixed to the inner roof of an oven, and its bottom is connected to a carbon fiber rod, whose top end comes out from the vent hole of the oven. We place a marker at the top of the carbon fiber rod and use a laser displacement sensor (OPT2006, Wenglor sensoric GmbH) to *measure the TCA's contraction*. The weight of the carbon fiber rod with the marker is negligible (0.2 g). In an experiment, a weight is hanged at the bottom of a TCA: 2 g, 30 g, and 60 g for the free-stroke TCA; 50 g, 100 g, and 200 g for the self-coiled TCA.

In the experiment, the temperature inside the oven slowly increases to 160°C from the room temperature (25°C) in around 14 mins, and the temperature is recorded with a thermistor (EPCOS Inc., B57540G0503F000). Due to the comparable sizes of the TCA and the thermistor and the slow increasing rate of the temperature, the TCA's temperature is approximately the temperature measured by the thermistor. Before an experiment, we place the corresponding weight and conduct a heating cycle (heat up and cool down) using electricity, and wait 3 mins to start an experiment. This process will allow the TCA to quickly creep to a length close to the equilibrium length corresponding to the weight. Comparing with heating a TCA with electricity and measuring the TCA's temperature, conducting experiments in an oven achieves better accuracy by eliminating environmental influence. The slow heating process also provides enough time for the thermistor to respond, and it also eliminates possible dynamic effects (inertial and damping) for the statics.

Figure 10(b) and (c) shows the comparison between experimental and simulation results using the rod model for the self-coiled TCA and the free-stroke TCA, respectively. The shaded area and the solid line are respectively the mean value and the standard deviation of three repeated measurements. The maximum standard deviation of all the static experiments for the two TCAs is 1.24 mm.

To quantify the accuracy of the three methods, the normalized displacement error (the difference between simulation and experimental results normalized by the maximum displacement of three experiments) for the three methods are calculated and plotted in Fig. 10(d), (e), and (f) for the self-coiled TCA with 50 g, 100 g, and 200 g, and in Fig. 10(g), (h), and (i) for the free-stroke TCA with 2 g, 30 g, and 60 g. The results indicate that in terms of accuracy: rod model > CST method > Love's method. For all three methods, the errors grow with the increase of the temperature and weight.

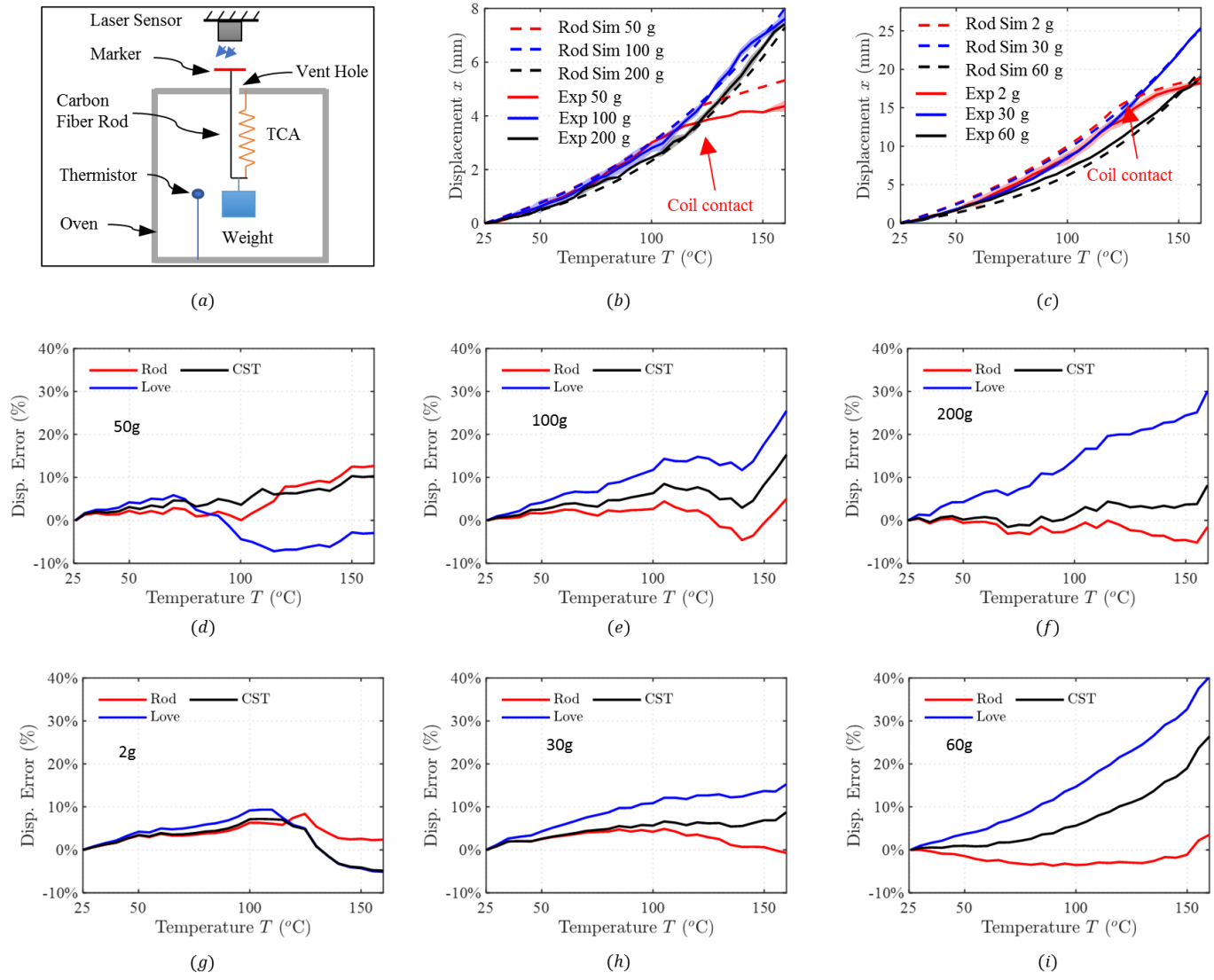


Fig. 10: Case 1: kinetostatics with a hanging weight. (a) Experimental setup. (b) The comparison between simulation results using the rod model and experimental results for the self-coiled TCA. (c) The comparison between simulation results using the rod model and experimental results for free-stroke TCA. (d), (e), and (f): The normalized displacement error of the simulations for the self-coiled TCA using the Cosserat rod model, Love's method and CST method respectively for 50 g, 100 g, and 200 g. (g), (h), and (i): The normalized displacement error of the simulations for the free-stroke TCA using the Cosserat rod model, Love's method and CST method respectively for 2 g, 30 g, and 60 g.

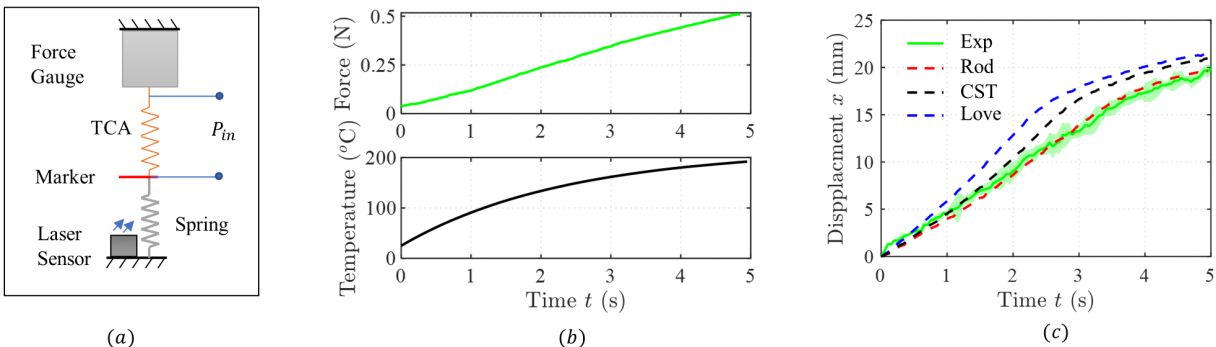


Fig. 11: Case 2: varying load. (a) Experimental setup. (b) The measured force and calculated temperature using the thermal model. (c) The comparison of the experimental results and the simulation results using the three methods.

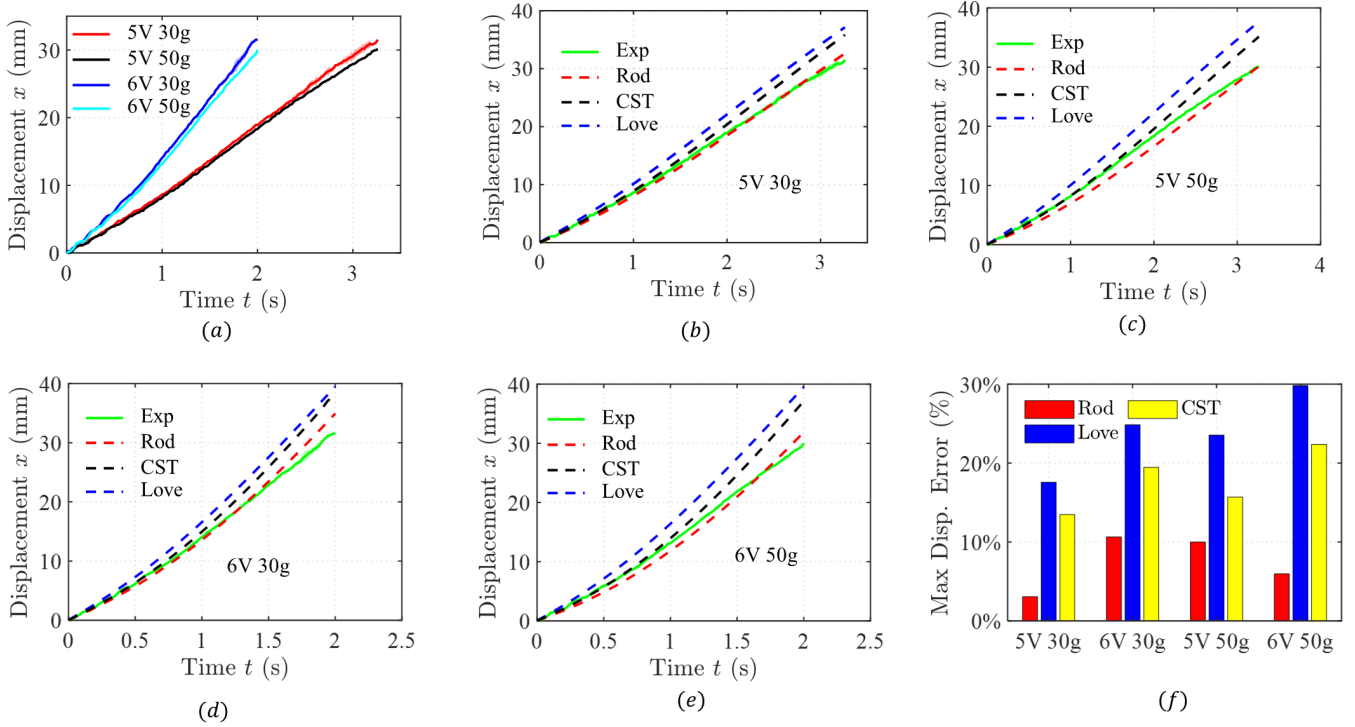


Fig. 12: *Case 3: Dynamics with a hanging weight.* (a) The experimental results for the four cases. (b)-(e) The experimental and the simulation results for 5V 30g, 5V 50g, 6V 30g, and 6V 50g cases. The shaded area of the green curve represents the standard deviation of three repeated experiments. (f) The maximum displacement error of the four cases for the three methods.

But the maximum error of the Cosserat rod model is less than 10 %, whereas the maximum error for Love's equation can be around 40 %. The potential reasons for the better accuracy of CST method than Love's method are 1) the CST method considers all the same four strains (torsion, bending, shear, and extension) as considered in the Cosserat rod model, but Love's methods only consider two strains (torsion and bending). 2) the numerical simulation of the CST method iteratively updates its parameters such as r and α . Even though the CST method is based on the infinitesimal strain theory, the numerical iteration improves its accuracy.

3) *Case 2: Varying Load:* After verifying the accuracy of the *kinetostatics* modeling, we connect a TCA with a mechanical spring to simulate a varying load when the TCA contracts. The varying load from the spring only depends on the displacement, not on time factors such as velocity or acceleration of the contraction (i.e., no dynamic effects). This case has many applications in TCA-driven robots. A typical case is a soft manipulator driven by embedded TCAs: the force on the TCA increases as the TCA contracts to bend the soft manipulator [60].

As shown in Fig. 11(a), one end of the spring is fixed, and its other end is attached to the TCA. The other end of the TCA is connected to a force gauge (M5-12, Mark-10 Inc.) to measure the real-time force during the experiments. To keep the TCA taut, a 0.05 N pretension is applied. The laser displacement sensor is used to record the TCA's displacement by measuring the displacement of a marker placed at the connection point between the TCA and the spring. The TCA is actuated using

5 V voltage, and its power is recorded using a high-side current/voltage sensor (INA 219, Adafruit), which is not a constant due to the change of the TCA's resistance during the actuation. In this experiment, only the free-stroke TCA is used since it can provide a large stroke without significant pretension. The recorded force and the calculated temperature using the thermal model are plotted in Fig. 11(b). Using the calculated temperature and the measured force, we solve the TCA's displacement using the three models. The comparison between the simulation and experimental results are shown in Fig. 11(c). *Each experiment is repeated three times, and the green shaded area represents the standard deviation (maximum std = 1.58 mm).* From the comparisons, the Cosserat rod model is still the most accurate modeling method.

4) *Case 3: Dynamics with a hanging weight:* Our final experiment for helical TCAs is to evaluate the accuracy of dynamics. In the experiments, a weight (30 g or 50 g) is hanged at the end of the free-stroke TCA (60 g is not used to prevent the TCA from breaking). A constant voltage (5 V or 6 V) is applied to the TCA. The power and displacement of the TCA are respectively measured as in previous experiments. Each experiment is repeated three times, and the results are shown in Fig. 12 (a). The maximum standard deviation for the four types of experiments is 0.84 mm. The comparison of the experimental and simulation results using the three methods for different combinations of weight and voltages are shown in Fig. 12 (b), (c), (d), and (e). With the rod model, the maximum displacement error normalized by the maximum displacement is less than 12% as shown in Fig. 12(f), which shows that the

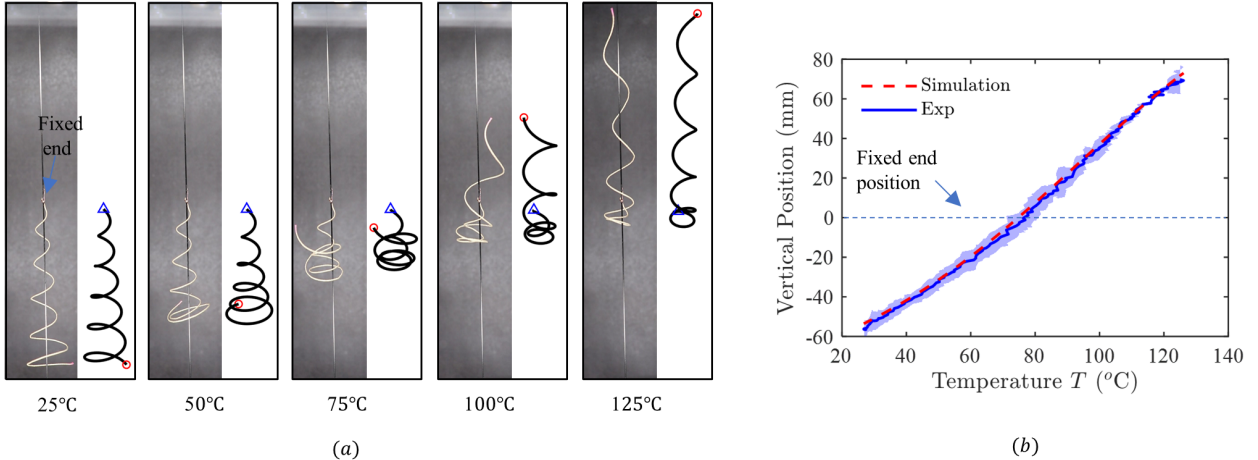


Fig. 13: The experimental and simulation results for the conical TCA. (a) Optical pictures of the conical TCA when heated in an oven compared with simulation results, showing the progression of actuation during heating. The free end is marked with a red circle and the fixed end is marked with a blue triangle. (b) The experimental and simulation results of the conical TCA's end point's vertical position with respect to temperature.

Cosserat rod method provide better accuracy compared with the other two methods.

E. Non-uniform Geometry Case: Kinetostatics of a Conical TCA

In this section, we demonstrate the capability of the Cosserat rod model to simulate TCAs of non-uniform geometry (conical TCAs). Conical TCAs can generate dual-side displacement and thus provide stroke over 100%. To make sure the coils can pass each other, the transverse gaps between coils are intentionally designed to be large and thus the load-bearing capability of the conical TCA is small. In our experiment, no load is applied to the end of the conical TCA during the experiments.

The conical TCA is fixed on a vertical carbon fiber rod placed in the oven with a transparent door, and a camera records the actuation of the conical TCA during the heating process. In our simulation, the fixed end is marked with a blue triangle and the free end is marked with a red circle. Figure 13(a) shows the optical pictures of the conical TCA and the corresponding simulated shapes for different temperatures (also see our supporting video). The comparison suggests the simulation can well capture the shape of the TCA. The minor error could be caused by the heated air flowing in the oven. The results seem surprising – the bigger coils pass the small coils and it does not exist a moment when all coils coincide on a plane (like a flat spiral). But it is reasonable since larger coils have a larger coil kinematic coefficient A and thus can generate more displacement if no load is applied.

The displacement of the TCA's free endpoint is extracted from the recorded video using Tracker software (<https://physlets.org/tracker>). Similarly, the temperature is recorded using the thermal sensor used for the helical TCA experiments. Figure 13(b) shows the comparison of the simulated and experimental vertical position of the TCA's free end

with respect to temperature. The maximum standard deviation for the three repeated experiments is 8.9 mm.

VI. DISCUSSIONS

Our proposed model based on the Cosserat rod model is a general and flexible framework. For generality, *besides the three type of TCAs discussed in this paper, the Cosserat rod model can be leveraged to model more complicated TCAs (e.g., TCA of ellipse-helical or logarithmic spiral shapes) as long as we can parametrize them along the twisted fiber. The framework can also be extended to model TCA-inspired artificial muscles (e.g., cavatapi [4] and dual-stroke artificial muscles [5] after the untwisting with respect to stimuli is obtained, and the framework can even be generalized to model stimuli-responsive materials (e.g., shape memory alloy coils) by incorporating memorized shapes and moduli change with respect to the stimuli.* For flexibility, this work contains some ‘complicated’ parts, but the Cosserat rod model can work without considering them for potentially fast computations at the expense of worse accuracy. For example, we considered the dependence of the moduli on temperature and strain, but we can use a constant E and G for the simulation. Note that the main contribution of this work is the general modeling framework for various types of TCAs made from the same twisted fiber. But if a different material or different parameters are used to fabricate the TCA, the properties for the twisted fiber need to be measured to obtain accurate results.

Although Cosserat rod model can provide better accuracy, especially with heavy load and high temperature (Fig. 10), the simplified methods (e.g., CST) on average can be computed 10 times faster. For example, the dynamics case using the rod model takes an average of 24 s for a simulation of 1 s while the other methods take around 2 s (all with a step size of 0.05 s running on an Intel Xeon E3-1245 CPU at 3.4GHz). In this case, the simplified models should be used when a TCA is subject to a small payload and low temperature. More

generally, based on the discussion in section IV, one can customize a simplified model by choosing A and K_c from either the Love's method or the CST method, or even choose to obtain A and K_c through measurement. In the future, however, the computation speed of using Cosserat rod method can be significantly improved by *using a discrete elastic rod method [61], [62], implementation in C++, and parallel computing*.

Besides the three loading cases, a TCA could subject to more complicated loading cases when used to actuate robots [60]. Our general framework for modeling TCAs can be leveraged for modeling these TCA-driven robots since it allows us to predict the output force and displacement that drive the robot to work. Such a general model even open the possibilities to model the performance of robots driven by TCAs of various shapes, for example robotic morphing skins driven by conical TCAs [25], which is impossible with other TCA modeling methods..

Finally, this paper focuses on modeling the exact mechanics of a TCA's actuation process *without considering the releasing process (i.e., when the temperature decreases). But the releasing can be modeled using the same mechanics model with different temperature profiles as verified by other works [16], [36]. In other words, a TCA's displacement is roughly the same for a specific temperature no matter it is in a releasing or actuation stage. And a TCA's temperature in the releasing stage can be predicted by the same thermal model (Eq. (1)) by setting $P_{in} = 0$. For a highly dynamic and cyclic situation, hysteresis and friction effect should be considered for control purposes [63], [64]. In our work, 'lonely stroke' [59] is accounted for by starting the simulation from a crept state, and dynamic hysteresis is described using a damping term that provided a modest approximation for its dynamic behavior. These considerations pave the way for advanced modeling of the nonlinear effects.*

VII. CONCLUSIONS

We have presented a general physics-based modeling framework for various types of TCAs using the Cosserat rod model. Compared with existing works, the model was able to not only provide more accurate results but also simulate TCAs with non-uniform geometries. We also showed that existing Love's and CST methods are two special simplified cases of a Cosserat rod model. This model paved the way to better understand the mechanics of TCAs as well as design TCAs to actuate a variety of robots/systems/devices. Our future work could attempt to improve model accuracy by incorporating additional effects, such as the creeping of the TCA and stress relaxation. Future work will also apply the model for TCA-driven robots, which involves interaction with the environment such as friction and contact forces.

APPENDIX A NOMENCLATURE

APPENDIX B DETAILED DERIVATION

A. Constitutive Law of a General Twisted Yarn

Based on the existing yarn mechanics theory, the twisted fiber is a transversely isotropic material, and its general stress-

Symbol	Unit	Definition
r_t	m	Twisted fiber radius
l_t	m	Length of the twisted fiber
α_t	rad	A twisted fiber's bias angle
E	Pa	Twisted fiber's longitudinal Young's modulus
G	Pa	Twisted fiber's longitudinal shear modulus
r	m	radius of a TCA
n_t	none	Number of twists in the twisted fiber
n		Number of the TCA's coils
ϕ	rad	Winding angle of the TCA $\phi = 2\pi n$
l	m	Length of the TCA
α	rad	The coil pitch angle of the TCA
\mathbf{M}_e		External moment vector applied at the boundary
\mathbf{F}_e		External force vector applied at the boundary
A		Coil kinematic coefficient
K_c		Coil stiffness coefficient
s	m	Arc length of a twisted fiber
t	sec	Time
\mathbf{p}	m	Position vector in the global frame
R		Rotational matrix of material cross section
\mathbf{h}		Quaternion for the material cross section
u	1/m	Angular strain in the body frame
v		Linear strain in the body frame
ξ		Spatial twist $\xi = [\mathbf{u}^T \ \mathbf{v}^T]^T$ in the body frame
\mathbf{m}		Internal moment in the body frame
\mathbf{n}		Internal contact force in the body frame
\mathbf{W}		Internal wrench $\mathbf{W}_i = [\mathbf{m}^T \ \mathbf{n}^T]^T$ in the body frame
$\bar{\mathbf{f}}$	N/m	Distributed force in the body frame
\bar{l}	N·m/m	Distributed moment in the body frame
$\bar{\mathbf{W}}_e$		Distributed external Wrench applied to the centerline in the body frame $\bar{\mathbf{W}}_e = [\bar{l}^T \ \bar{\mathbf{f}}^T]^T$
$\Delta(\cdot)$		The change of the variable with respect to the state defined by the superscripts
$(\cdot)^*$		Variables corresponding to the original reference state
$(\cdot)^h$		Variables corresponding to the heated reference state
$(\cdot)'$		Derivative with respect to s , $\frac{\partial}{\partial s}$
(\cdot)		Derivative with respect to time, $\frac{\partial}{\partial t}$
$\ddot{(\cdot)}$		Derivative with respect to time, $\frac{\partial^2}{\partial t^2}$
$\hat{\cdot}$ or $(\cdot)\hat{\cdot}$		Mapping from \mathbb{R}^3 to $\mathfrak{so}(3)$ or \mathbb{R}^6 to $\mathfrak{se}(3)$, e.g.
$\hat{\xi} = \begin{bmatrix} \hat{\mathbf{u}} & \hat{\mathbf{v}} \\ \mathbf{0} & 0 \end{bmatrix}$, $\hat{\mathbf{u}} = \begin{bmatrix} 0 & -u_z & u_y \\ u_z & 0 & -u_x \\ -u_y & u_x & 0 \end{bmatrix}$		
$\check{\cdot}$ or $(\cdot)\check{\cdot}$		Inverse of $\hat{\cdot}$ or $(\cdot)\hat{\cdot}$

TABLE IV: Nomenclature

strain relationships is the following [51]

$$\begin{bmatrix} \epsilon_x \\ \epsilon_y \\ \epsilon_z \\ \gamma_{xy} \\ \gamma_{yz} \\ \gamma_{xz} \end{bmatrix} = \begin{bmatrix} \frac{1}{E_T} & \frac{-\nu_{TT}}{E_T} & \frac{-\nu_{LT}}{E_L} & 0 & 0 & 0 \\ \frac{-\nu_{TT}}{E_T} & \frac{1}{E_T} & \frac{-\nu_{LT}}{E_L} & 0 & 0 & 0 \\ \frac{-\nu_{TL}}{E_T} & \frac{-\nu_{TL}}{E_T} & \frac{1}{E_L} & 0 & 0 & 0 \\ 0 & 0 & 0 & \frac{1}{G_T} & 0 & 0 \\ 0 & 0 & 0 & 0 & \frac{1}{G_{TL}} & 0 \\ 0 & 0 & 0 & 0 & 0 & \frac{1}{G_{TL}} \end{bmatrix} \begin{bmatrix} \sigma_x \\ \sigma_y \\ \sigma_z \\ \tau_{xy} \\ \tau_{yz} \\ \tau_{xz} \end{bmatrix} \quad (34)$$

where the subscripts T and L respectively represent the transverse direction (x or y) and longitudinal direction (z). ϵ 's and γ 's are normal and shear stress, and σ 's and τ 's are normal and shear strains in mechanics convention. E_L is the longitudinal modulus governing uniaxial loading in the z direction, ν_{LT} is the associated Poisson's ratio governing induced transverse strains, E_T is the transverse modulus governing uniaxial strains in the transverse direction, ν_{TL} is the associated

Poisson's ratio governing induced longitudinal strains and ν_{TT} is the associated Poisson's ratio governing resultant strains in the remaining orthogonal transverse direction, G_{TL} is the longitudinal shear modulus governing shear in the longitudinal direction, and G_T is the transverse shear modulus governing shear in the transverse plane.

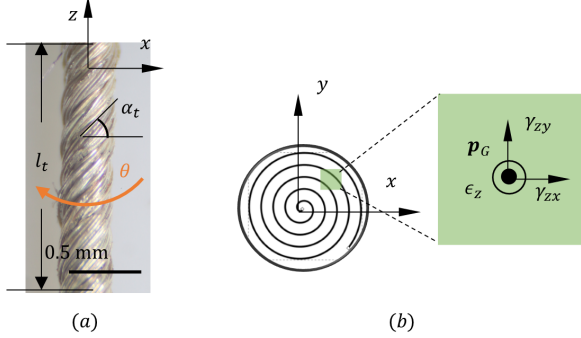


Fig. 14: (a) The microscopic photo of a twisted fiber. (b) Cross section of the twisted fiber taken at the $x - y$ plane of the body frame. Strain quantities on this face of a small volume element at point p_G are shown.

The twisted fiber's mechanical properties depend on its filament direction α_f as shown in Fig. 14(a). The Cosserat rod model assumes a rigid cross-section; therefore, ϵ_x , ϵ_y and γ_{xy} do not exist, and the constitutive relation for the transversely isotropic rod reduces to:

$$\sigma_z = E\epsilon_z, \tau_{zx} = G\gamma_{zx}, \tau_{zy} = G\gamma_{zy} \quad (35)$$

where for simplicity, we use $E = E_L$ is the longitudinal Young's modulus, and $G = G_{TL}$ is the longitudinal shear modulus. The strains can be related to the independent variables \mathbf{v} and \mathbf{u} : $[\gamma_{zx}, \gamma_{zy}, \epsilon_z]^T = \Delta\mathbf{v} - \mathbf{p}_G \times \Delta\mathbf{u}$ where $\mathbf{p}_G = [x, y, 0]^T$ is the position of the element within the cross section as shown in Fig. 14(b), $\Delta\mathbf{v} = \mathbf{v} - \mathbf{v}^*$ and $\Delta\mathbf{u} = \mathbf{u} - \mathbf{u}^*$, and the values with *, \mathbf{v}^* and \mathbf{u}^* , are respectively the values of \mathbf{v} and \mathbf{u} in the ORS. Manipulating these equations, we can establish a relationship between $\Delta\xi$ and \mathbf{W} which simplifies to Eq. (8).

B. Identify h in Eq. (1) and λ in Eq. (11)

To identify h in Eq.(1), we first conduct a statics experiment to infer the actual $T - t$ (temperature-time) relationship of a dynamics experiment, and then use the $T - t$ relationship to identify h . For the statics experiment, We slowly heat up a free-stroke TCA with a 60 g at the end in an oven while measuring the $T - x$ (temperature – displacement) relationship. The 60 g (the maximum weight used in our manuscript) will prevent the coils from early contact. After that, we can conduct the dynamics experiment and obtain the $x - t$ relationship of a TCA by applying a constant voltage (5 V). Using the $T - x$ and $x - t$ relationships, we can infer the temperature of the dynamic experiment to obtain the $T - t$ relationship using a linear interpolation (interp1 in Matlab).

With the $T - t$ relationship, we can perform a linear regression to obtain h . Specifically, we formulated an optimization problem: Minimize: $RMSE(h) =$

$\sqrt{\sum_{i=1}^n (T_{exp,i} - T_{sim,i}(h))^2 / n}$, to find the value h that minimizes the root mean square error between the experimental and simulation results.

$\lambda = \mu_2\tau^2 + \mu_1\tau + \mu_0$ in Eq. (11) determines how the strain moduli will change due to large external load under high temperature. The coefficients μ_0, μ_1, μ_2 are solved using three pair of values $[\tau_1, \lambda_1], [\tau_2, \lambda_2], [\tau_3, \lambda_3]$, corresponding to three different external loads (0 g, 30 g, and 60 g) applied to the TCA, which are identified through an experiment using a free stroke TCA. We choose 30 g and 60 g because 60 g is the largest load for the TCA in this work and 30 g is the half of the maximum load, over which the moduli changes become significant based on our observations. Since the moduli only drop significantly when the temperature and load are high, we measure the displacement of the TCA at the highest temperature ($160^\circ C$). When there is no load, we have $[\tau_1, \lambda_1] = [0, 1]$, which means the change of E_f in Eq. (11) is only from the increase of the temperature. When there is a 30 g load, we can obtain $\lambda_2 = 1$ by assuming that there is no moduli change from no load to 30 g. Based on the linear strain deformation theory, $\tau_3 - \tau_2 = \tau_2 - \tau_1$, therefore, $\tau_2 = \tau_3/2$.

When there is a 60 g load, we solve the corresponding $[\tau_3, \lambda_3]$ as follows. We first calculate the shear modulus corresponding to 60 g using a linear relationship $G_{60} = (l_{tr}^2 \cos \alpha_{30}) / (\Delta x J) \Delta Fe$, where Δx is the displacement of the TCA when a weight is increased from 30 g to 60 g, and α_{30} is the pitch angle for the situation with 30 g. $\lambda_3 = 5.68$ can be reversely calculated using Eq. (10) and Eq. (11) with known G_{60} . To obtain the torsional strain τ_3 , we first calculate the pitch angle α_{60} using the displacement, and then the torsion strain change with respect to the situation of 30 g can be calculated using $\tau_3 - \tau_2 = (\sin 2\alpha_{60} - \sin 2\alpha_{30}) / 2r \approx 85.5$ (similar to Eq. (19)). Therefore, $[\tau_3, \lambda_3] = [171, 5.68]$ and $[\tau_2, \lambda_2] = [85.5, 1]$. We can find the coefficients μ_2 , μ_1 , and μ_0 using polyfit in Matlab by fitting the three points.

C. The Reference Twist and Boundary Condition for Conical TCAs

We fabricate the conical TCA in conical Archimedes's spiral shape

$$\mathbf{p}^*(z) = [bz \cos(az), bz \sin(az), z]^T \quad (36)$$

where z is the vertical height, b is radial scaling factor, and a is angular scaling factor.

To establish initial and boundary condition for the rod model, the rod geometry needs to be parameterized using arc length s that can be easily derived by integrating the derivative of the position vector with respect to z

$$s(z) = \int_0^z \left| \frac{d\mathbf{p}^*}{dz} \right| dz = \frac{1}{2} z \sqrt{1 + b^2(1 + a^2 z^2)} + \frac{1 + b^2}{2ab} \sinh^{-1} \left(\frac{abz}{\sqrt{1 + z^2}} \right) \quad (37)$$

To use the Cosserat rod model, the curve needs to be parameterized using s . However, z in Eq. (37) cannot be analytically solved and there is no explicit form to express \mathbf{p} in terms of s as done for a helix in Eq. (12).

To solve this problem, we discrete the spiral into N segments and numerically find z_i for a specific s_i ($i \in [1, N]$) by solving $s(z_i) = s_i$ using Eq.(37) by a root searching method (*fzero()* in Matlab). At the end of i^{th} segment, the curvature and the torsion of the spiral can be found by

$$\kappa^*(z_i) = \frac{abz\sqrt{4 + a^2z_i^2 + b^2(2 + a^2b^2)^2}}{(1 + b^2(1 + a^2z^2))^{3/2}} \quad (38)$$

$$\tau^*(z_i) = \frac{a(6 + a^2z_i^2)}{4 + a^2z_i^2 + b^2(2 + a^2z_i^2)^2} \quad (39)$$

The global frame's Z direction along the centerline of the helical spiral; the body frame's z direction is along tangent direction of the curve and the cross section is in the x - y plane. The heated reference strain

$$\mathbf{u}^h(z_i) = \begin{bmatrix} 0 \\ \kappa(z_i) \\ \tau(z_i)^* + \Delta\bar{\theta}^h \end{bmatrix}, \mathbf{v}^h = \mathbf{v}^* = [0, 0, 1]^T \quad (40)$$

The initial orientation and position for $s_i = 0$ are

$$\mathbf{p}_0 = [0, 0, 0]^T, R_0 = R_z(\pi + 0.1) \quad (41)$$

The boundary condition for the free end is $\mathbf{W}(l_t) = [0, 0, 0, 0, 0, 0]^T$ since no load is applied.

D. Kinetostatic Modeling using CST

In our previous work [32], CST is directly used to model a TCA. Here we present a more concise derivation compared with Ref. [32]. The actuation is considered as an external force, $M_a = \Delta\theta^h GJ$ applied along z axis, which means $M_z = -F_e r \cos \alpha - M_e \sin \alpha + M_a$ in \mathbf{W} . The complementary strain energy will be equal to the strain energy under the small deformation assumption leading to [65]

$$\begin{aligned} U^* &= \int_0^{l_t} (\mathbf{W}^T K^{-1} \mathbf{W}) ds \\ &= \int_0^{l_t} \left[\frac{M_z^2}{2GJ} + \frac{M_y^2}{2EI} + \frac{F_y^2}{2GA_t} + \frac{F_z^2}{2EA_t} \right] ds \end{aligned} \quad (42)$$

where U^* is the complimentary strain energy. Notice that six deformation terms are reduced to four terms since $M_x = 0$ and $F_x = 0$. M_e is not considered and after we apply CST $\frac{dU^*}{dF_e} = l^* - l$, it will arrive Eq. (29).

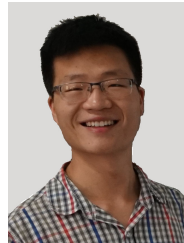
ACKNOWLEDGMENT

The authors would like to thank Ben Pawlowski and Dr. John Till for intellectual discussions on Cosserat rod model simulation, and Brandon Tighe for updating our customized TCA machine for fabricating TCAs.

REFERENCES

- [1] C. S. Haines, M. D. Lima, N. Li, G. M. Spinks, J. Foroughi, J. D. Madden, S. H. Kim, S. Fang, M. J. de Andrade, F. Göktepe, *et al.*, "Artificial muscles from fishing line and sewing thread," *science*, vol. 343, no. 6173, pp. 868–872, 2014.
- [2] J. Mu, M. J. De Andrade, S. Fang, X. Wang, E. Gao, N. Li, S. H. Kim, H. Wang, C. Hou, Q. Zhang, *et al.*, "Sheath-run artificial muscles," *Science*, vol. 365, no. 6449, pp. 150–155, 2019.
- [3] H. Chu, X. Hu, Z. Wang, J. Mu, N. Li, X. Zhou, S. Fang, C. S. Haines, J. W. Park, S. Qin, N. Yuan, J. Xu, S. Tawfick, H. Kim, P. Conlin, M. Cho, K. Cho, J. Oh, S. Nielsen, K. A. Alberto, J. M. Razal, J. Foroughi, G. M. Spinks, S. J. Kim, J. Ding, J. Leng, and R. H. Baughman, "Unipolar stroke, electroosmotic pump carbon nanotube yarn muscles," *Science*, vol. 371, no. 6528, pp. 494–498, 2021.
- [4] D. R. Higueras-Ruiz, M. W. Shafer, and H. P. Feigenbaum, "Cavatappi artificial muscles from drawing, twisting, and coiling polymer tubes," *Science Robotics*, vol. 6, no. 53, 2021.
- [5] G. M. Spinks, N. D. Martino, S. Naficy, D. J. Shepherd, and J. Foroughi, "Dual high-stroke and high-work capacity artificial muscles inspired by dna supercoiling," *Science Robotics*, vol. 6, no. 53, 2021.
- [6] S. M. Mirvakili, A. R. Ravandi, I. W. Hunter, C. S. Haines, N. Li, J. Foroughi, S. Naficy, G. M. Spinks, R. H. Baughman, and J. D. Madden, "Simple and strong: Twisted silver painted nylon artificial muscle actuated by joule heating," in *Electroactive Polymer Actuators and Devices (EAPAD) 2014*, vol. 9056. International Society for Optics and Photonics, 2014, p. 90560I.
- [7] A. Abbas and J. Zhao, "Twisted and coiled sensor for shape estimation of soft robots," in *2017 IEEE/RSJ International Conference on Intelligent Robots and Systems (IROS)*, Sept 2017, pp. 482–487.
- [8] J. van der Weijde, H. Vallery, and R. Babuška, "Closed-loop control through self-sensing of a joule-heated twisted and coiled polymer muscle," *Soft robotics*, vol. 6, no. 5, pp. 621–630, 2019.
- [9] J. Sun and J. Zhao, "Integrated actuation and self-sensing for twisted-and-coiled actuators with applications to innervated soft robots," in *2020 IEEE International Conference on Robotics and Automation (ICRA)*, 2018, pp. 5912–5917.
- [10] D. Bombara, S. Fowzer, and J. Zhang, "Compliant, large-strain, and self-sensing twisted string actuators," *Soft Robotics*, 2020.
- [11] J. Sun, B. Pawlowski, and J. Zhao, "Soft manipulators with programmable motion using twisted-and-coiled actuators (conference presentation)," in *Electroactive Polymer Actuators and Devices (EAPAD) XXI*, vol. 10966. International Society for Optics and Photonics, 2019, p. 109660Q.
- [12] J. Sun, B. Tighe, Y. Liu, and J. Zhao, "Twisted-and-coiled actuators with free strokes enable soft robots with programmable motions," *Soft Robotics*, 2020.
- [13] C. S. Haines, N. Li, G. M. Spinks, A. E. Aliev, J. Di, and R. H. Baughman, "New twist on artificial muscles," *Proceedings of the National Academy of Sciences*, vol. 113, no. 42, pp. 11709–11716, 2016.
- [14] L. Sutton, H. Moein, A. Rafiee, J. D. Madden, and C. Menon, "Design of an assistive wrist orthosis using conductive nylon actuators," in *Biomedical Robotics and Biomechatronics (BioRob), 2016 6th IEEE International Conference on*. IEEE, 2016, pp. 1074–1079.
- [15] L. Wu, M. J. de Andrade, L. K. Saharan, R. S. Rome, R. H. Baughman, and Y. Tadesse, "Compact and low-cost humanoid hand powered by nylon artificial muscles," *Bioinspiration & biomimetics*, vol. 12, no. 2, p. 026004, 2017.
- [16] M. C. Yip and G. Niemeyer, "On the control and properties of supercoiled polymer artificial muscles," *IEEE Transactions on Robotics*, vol. 33, no. 3, pp. 689–699, 2017.
- [17] K. H. Cho, M. G. Song, H. Jung, J. Park, H. Moon, J. C. Koo, J.-D. Nam, and H. R. Choi, "A robotic finger driven by twisted and coiled polymer actuator," in *Electroactive Polymer Actuators and Devices (EAPAD) 2016*, vol. 9798. International Society for Optics and Photonics, 2016, p. 97981J.
- [18] L. Wu, I. Chauhan, and Y. Tadesse, "A novel soft actuator for the musculoskeletal system," *Advanced Materials Technologies*, vol. 3, no. 5, p. 1700359, 2018.
- [19] K. H. Cho, H. S. Jung, S. Y. Yang, Y. Kim, H. Rodrigue, H. Moon, J. C. Koo, and H. R. Choi, "Sliding filament joint mechanism: biomimetic artificial joint mechanism for artificial skeletal muscles," *Journal of Mechanisms and Robotics*, vol. 11, no. 2, 2019.
- [20] J. Sun, B. Pawlowski, and J. Zhao, "Embedded and controllable shape morphing with twisted-and-coiled actuators," in *2018 IEEE/RSJ International Conference on Intelligent Robots and Systems (IROS)*, Oct 2018, pp. 5912–5917.
- [21] J. Zhang, "Modeling of a bending supercoiled polymer (scp) artificial muscle," *IEEE Robotics and Automation Letters*, vol. 5, no. 3, pp. 3822–3829, 2020.
- [22] X. Tang, K. Li, Y. Liu, D. Zhou, and J. Zhao, "A soft crawling robot driven by single twisted and coiled actuator," *Sensors and Actuators A: Physical*, vol. 291, pp. 80–86, 2019.
- [23] Y. Yang, Y. A. Tse, Y. Zhang, Z. Kan, and M. Y. Wang, "A low-cost inchworm-inspired soft robot driven by supercoiled polymer artificial

- muscle,” in *2019 2nd IEEE International Conference on Soft Robotics (RoboSoft)*. IEEE, 2019, pp. 161–166.
- [24] Y. Almubarak and Y. Tadesse, “Twisted and coiled polymer (tcp) muscles embedded in silicone elastomer for use in soft robot,” *International Journal of Intelligent Robotics and Applications*, vol. 1, no. 3, pp. 352–368, 2017.
- [25] C. Lamuta, H. He, K. Zhang, M. Rogalski, N. Sottos, and S. Tawfick, “Digital texture voxels for stretchable morphing skin applications,” *Advanced Materials Technologies*, vol. 4, no. 8, p. 1900260, 2019.
- [26] A. Hamidi, Y. Almubarak, Y. M. Rupawat, J. Warren, and Y. Tadesse, “Poly-saora robotic jellyfish: swimming underwater by twisted and coiled polymer actuators,” *Smart Materials and Structures*, vol. 29, no. 4, p. 045039, 2020.
- [27] Q. Yang and G. Li, “A top-down multi-scale modeling for actuation response of polymeric artificial muscles,” *Journal of the Mechanics and Physics of Solids*, vol. 92, pp. 237–259, 2016.
- [28] K. H. Cho, M.-G. Song, H. Jung, S. Y. Yang, H. Moon, J. C. Koo, H. R. Choi, et al., “Fabrication and modeling of temperature-controllable artificial muscle actuator,” in *2016 6th IEEE International Conference on Biomedical Robotics and Biomechatronics (BioRob)*. IEEE, 2016, pp. 94–98.
- [29] C. Oiwa, K. Masuya, K. Tahara, T. Irisawa, M. Shioya, T. Yamauchi, E. Tanaka, K. Asaka, and K. Takagi, “Gray-box modeling and control of torsional fishing-line artificial muscle actuators,” in *Electroactive Polymer Actuators and Devices (EAPAD) XX*, vol. 10594. International Society for Optics and Photonics, 2018, p. 1059428.
- [30] T. Luong, K. Kim, S. Seo, J. H. Park, Y. Kim, S. Y. Yang, K. H. Cho, J. C. Koo, H. R. Choi, and H. Moon, “Modeling and position control of a high performance twisted-coiled polymer actuator,” in *2018 15th International Conference on Ubiquitous Robots (UR)*. IEEE, 2018, pp. 73–79.
- [31] K. Masuya, S. Ono, K. Takagi, and K. Tahara, “Modeling framework for macroscopic dynamics of twisted and coiled polymer actuator driven by joule heating focusing on energy and convective heat transfer,” *Sensors and Actuators A: Physical*, vol. 267, pp. 443–454, 2017.
- [32] A. Abbas and J. Zhao, “A physics based model for twisted and coiled actuator,” in *Robotics and Automation (ICRA), 2017 IEEE International Conference on*. IEEE, 2017, pp. 6121–6126.
- [33] C. Lamuta, S. Messelot, and S. Tawfick, “Theory of the tensile actuation of fiber reinforced coiled muscles,” *Smart Materials and Structures*, vol. 27, no. 5, p. 055018, 2018.
- [34] N. Naik and V. Madhavan, “Twisted impregnated yarns: elastic properties,” *The Journal of Strain Analysis for Engineering Design*, vol. 35, no. 2, pp. 83–91, 2000.
- [35] C. Wu and W. Zheng, “A modeling of twisted and coiled polymer artificial muscles based on elastic rod theory,” in *Actuators*, vol. 9, no. 2. Multidisciplinary Digital Publishing Institute, 2020, p. 25.
- [36] F. Karami, L. Wu, and Y. Tadesse, “Modeling of one-ply and two-ply twisted and coiled polymer (tcp) artificial muscles,” *IEEE/ASME Transactions on Mechatronics*, pp. 300–310, 2020.
- [37] P. Kotak, T. Weerakkody, and C. Lamuta, “Physics-based dynamic model for the electro-thermal actuation of bio-inspired twisted spiral artificial muscles (tsams),” *Polymer*, vol. 222, p. 123642, 2021.
- [38] K. Masuya, S. Ono, K. Takagi, and K. Tahara, “Nonlinear dynamics of twisted and coiled polymer actuator made of conductive nylon based on the energy balance,” in *2017 IEEE International Conference on Advanced Intelligent Mechatronics (AIM)*. IEEE, 2017, pp. 779–784.
- [39] F. Karami and Y. Tadesse, “Modeling of twisted and coiled polymer (tcp) muscle based on phenomenological approach,” *Smart Materials and Structures*, vol. 26, no. 12, p. 125010, 2017.
- [40] S. Aziz, S. Naficy, J. Foroughi, H. R. Brown, and G. M. Spinks, “Controlled and scalable torsional actuation of twisted nylon 6 fiber,” *Journal of Polymer Science Part B: Polymer Physics*, vol. 54, no. 13, pp. 1278–1286, 2016.
- [41] S. Aziz and G. M. Spinks, “Torsional artificial muscles,” *Materials Horizons*, vol. 7, no. 3, pp. 667–693, 2020.
- [42] A. E. H. Love, *A treatise on the mathematical theory of elasticity*. Cambridge university press, 1944.
- [43] V. Giovinco, P. Kotak, V. Cichella, C. Maletta, and C. Lamuta, “Dynamic model for the tensile actuation of thermally and electro-thermally actuated twisted and coiled artificial muscles (tcams),” *Smart Materials and Structures*, vol. 29, no. 2, p. 025004, 2019.
- [44] A. M. Wahl, *Mechanical springs*. Penton Publishing Company, 1944.
- [45] S. Antman, *Nonlinear Problems of Elasticity, volume 107 of Applied Mathematical Sciences, 2nd edn.* Springer, 2005.
- [46] O. M. O'Reilly, *Modeling Nonlinear Problems in the Mechanics of Strings and Rods*. Springer, 2017.
- [47] D. C. Rucker and R. J. Webster III, “Statics and dynamics of continuum robots with general tendon routing and external loading,” *IEEE Transactions on Robotics*, vol. 27, no. 6, pp. 1033–1044, 2011.
- [48] F. Renda, M. Giorelli, M. Calisti, M. Cianchetti, and C. Laschi, “Dynamic model of a multibending soft robot arm driven by cables,” *IEEE Transactions on Robotics*, vol. 30, no. 5, pp. 1109–1122, 2014.
- [49] J. Till, V. Alois, and C. Rucker, “Real-time dynamics of soft and continuum robots based on cosserat rod models,” *The International Journal of Robotics Research*, vol. 38, no. 6, pp. 723–746, 2019.
- [50] C. Choy, W. Leung, and E. Ong, “Thermal expansivity of oriented nylon-6 and nylon-6, 6,” *Polymer*, vol. 26, no. 6, pp. 884–888, 1985.
- [51] N. Pan and D. Brookstein, “Physical properties of twisted structures. ii. industrial yarns, cords, and ropes,” *Journal of applied polymer science*, vol. 83, no. 3, pp. 610–630, 2002.
- [52] A. Demšar, V. Bukošek, and A. Kljun, “Dynamic mechanical analysis of nylon 66 cord yarns,” *Fibres & Textiles in Eastern Europe*, 2010.
- [53] C. Rucker, “Integrating rotations using nonunit quaternions,” *IEEE Robotics and Automation Letters*, vol. 3, no. 4, pp. 2979–2986, 2018.
- [54] I. Y. Bar-Itzhack, “New method for extracting the quaternion from a rotation matrix,” *Journal of guidance, control, and dynamics*, vol. 23, no. 6, pp. 1085–1087, 2000.
- [55] J. Kierzenka and L. F. Shampine, “A bvp solver that controls residual and error,” *JNAIAM J. Numer. Anal. Ind. Appl. Math*, vol. 3, no. 1-2, pp. 27–41, 2008.
- [56] H. Lomax, T. H. Pulliam, and D. W. Zingg, *Fundamentals of computational fluid dynamics*. Springer Science & Business Media, 2013.
- [57] S. Kianzad, M. Pandit, A. Bahi, A. Rafiee, F. Ko, G. M. Spinks, and J. D. Madden, “Nylon coil actuator operating temperature range and stiffness,” in *Electroactive Polymer Actuators and Devices (EAPAD) 2015*, vol. 9430. International Society for Optics and Photonics, 2015, p. 94301X.
- [58] P. Kelly, “Solid mechanics part i: An introduction to solid mechanics.” *A Creative Commons Attributions, Mountain View, CA*, vol. 94042, 2013.
- [59] R. Konda and J. Zhang, “Experimental investigation of the lonely stroke behavior in supercoiled polymer artificial muscles,” in *Electroactive Polymer Actuators and Devices (EAPAD) XXII*, vol. 11375. International Society for Optics and Photonics, 2020, p. 113751I.
- [60] B. Pawłowski, J. Sun, J. Xu, Y. Liu, and J. Zhao, “Modeling of soft robots actuated by twisted-and-coiled actuators,” *IEEE/ASME Transactions on Mechatronics*, 2018.
- [61] M. Bergou, M. Wardetzky, S. Robinson, B. Audoly, and E. Grinspun, “Discrete elastic rods,” in *ACM SIGGRAPH 2008 papers*, 2008, pp. 1–12.
- [62] M. K. Jawed, A. Novelia, and O. M. O'Reilly, *A primer on the kinematics of discrete elastic rods*. Springer, 2018.
- [63] J. Zhang, K. Iyer, A. Simeonov, and M. C. Yip, “Modeling and inverse compensation of hysteresis in supercoiled polymer artificial muscles,” *IEEE Robotics and Automation Letters*, vol. 2, no. 2, pp. 773–780, 2017.
- [64] J. Zhang, A. Simeonov, and M. C. Yip, “Three-dimensional hysteresis compensation enhances accuracy of robotic artificial muscles,” *Smart Materials and Structures*, vol. 27, no. 3, p. 035002, 2018.
- [65] C. L. Dym, “Consistent derivations of spring rates for helical springs,” *Journal of Mechanical Design*, vol. 131, no. 7, 2009.



Jiefeng Sun (S'19) received his B.S. in Mechanical Engineering in 2014 from Lanzhou University of Technology, and his M.S. degree in Mechanical Engineering in 2017 from Dalian University of Technology, China. He is currently a Ph.D. student of Mechanical Engineering in Colorado State University.

His current research interests include artificial muscle, soft robots and reconfigurable robots.



Jianguo Zhao (M'15) received the B.E. degree in mechanical engineering from Harbin Institute of Technology, Harbin, China, and the M.E. degree in mechatronic engineering from Shenzhen Graduate School, Harbin Institute of Technology, Shenzhen, China, in 2005 and 2007, respectively. He received the Ph.D. degree in electrical engineering from Michigan State University, East Lansing, MI, USA, in 2015. He is currently an Assistant Professor with Colorado State University, Fort Collins, CO, USA.

His research interests include bioinspired robotics, dynamics and control, and vision-based control.